



**Michigan
Technological
University**

Michigan Technological University
Digital Commons @ Michigan Tech

Dissertations, Master's Theses and Master's Reports

2022

Adapting Deep Learning for Underwater Acoustic Communication Channel Modeling

Li Wei

Michigan Technological University, liwei@mtu.edu

Copyright 2022 Li Wei

Recommended Citation

Wei, Li, "Adapting Deep Learning for Underwater Acoustic Communication Channel Modeling", Open Access Dissertation, Michigan Technological University, 2022.
<https://doi.org/10.37099/mtu.dc.etdr/1497>

Follow this and additional works at: <https://digitalcommons.mtu.edu/etdr>



Part of the [Hardware Systems Commons](#), [Other Computer Engineering Commons](#), [Other Electrical and Computer Engineering Commons](#), [Signal Processing Commons](#), and the [Systems and Communications Commons](#)

ADAPTING DEEP LEARNING FOR UNDERWATER ACOUSTIC
COMMUNICATION CHANNEL MODELING

By

Li Wei

A DISSERTATION

Submitted in partial fulfillment of the requirements for the degree of

DOCTOR OF PHILOSOPHY

In Electrical Engineering

MICHIGAN TECHNOLOGICAL UNIVERSITY

2022

© 2022 Li Wei

This dissertation has been approved in partial fulfillment of the requirements for the Degree of DOCTOR OF PHILOSOPHY in Electrical Engineering.

Department of Electrical and Computer Engineering

Dissertation Advisor: *Dr. Zhaohui Wang*

Committee Member: *Dr. Laura E. Brown*

Committee Member: *Dr. Xiaoyong Yuan*

Committee Member: *Dr. Jianhui Yue*

Department Chair: *Dr. Jin W. Choi*

Dedication

To my mother Zhulin Xiang, my father Yumin Wei, and Prof.
Mario Gerla (1943 - 2019)

who granted me the courage to change the things I can.

Contents

List of Figures	xi
List of Tables	xv
Acknowledgments	xvii
List of Abbreviations	xix
Abstract	xxi
1 Introduction	1
2 An Experiment Test-bed for Underwater Acoustic Communication and Networking	13
2.1 Related work on UWA test-bed system	15
2.2 Test-bed system design	16
2.3 UWA channel test capability	19
2.4 UWA networking test capability	20
2.5 Summary of the test-bed system	20

3	An Experimental Study of Underwater Acoustic Channel Impulse Response Distributions in the Keweenaw Waterway	21
3.1	Related work on the experimental study of UWA channel	23
3.2	Experiment Design	25
3.2.1	Transmitted OFDM Waveform	26
3.2.2	Experiment transmission Procedure	27
3.3	Field Experiment Results and analysis	29
3.3.1	Data obtained	29
3.3.2	Channel Impulse Response Results and Analysis	31
3.3.3	The Arrival Time Distributions of Significant Taps	31
3.3.4	The Main Tap Gain Distributions	32
3.4	Case Study 3.1: UWA Channel affected by Water Temperature Distribution	35
3.5	Case Study 3.2: Water Surface Condition	40
3.6	Case Study 3.3: Flood	45
3.7	Case Study 3.4: Ice Eater	45
3.8	Summary of the experiment	48
4	A Deep Generative Model for Underwater Acoustic Channel Impulse Response	49
4.1	Related Work	51

4.2	Wasserstein Conditional Generative Adversarial Network for UWA	
	CIR	54
4.3	Training the WCGAN	57
4.4	Power weighted JSD	62
4.5	Tuning the conditional variable for generating	64
4.6	Summary of the WCGAN	66
5	Prediction of the CIR distribution	67
5.1	Related Work	68
5.2	CGAN based prediction model for UWA CIR	71
5.3	Training the prediction CGAN	74
5.4	The prediction test results	79
5.5	Summary of the prediction model	82
6	Conclusions and Future works	83
	References	85

List of Figures

1.1	The workflow of a cognitive communication system [1]	6
2.1	Schematic diagram of the experiment system	16
2.2	Field node control box	18
2.3	Weather station sensor	18
3.1	The transmitted OFDM waveform	26
3.2	Deployment locations of the acoustic modems	28
3.3	Histogram of arrival times of significant taps	32
3.4	An example of the histogram of the main peak gains in a 1-hour time window	34
3.5	Histogram fit examples with different JSD	34
3.6	An example of the JSD trend	35
3.7	Case Study 3.1 weather information and communication performances (Row 1: Air temperature and solar radiation; Row 2: Wind speed and precipitation rate; Row 3: Packet loss ratio and packet header PSNR; Row 4: data block BER. Left column: Summer sunny days; middle column: Summer cloudy days; Right column: Winter open water) .	37

3.8	Air temperature and solar radiation	39
3.9	Hourly water temperature range	39
3.10	Hourly sound speed range	39
3.11	BELLHOP simulation with SSP measured at 2022-06-17 21:59 . . .	41
3.12	BELLHOP simulation with SSP measured at 2022-06-18 01:00 . . .	41
3.13	BELLHOP simulation with SSP measured at 2020-03-06 17:40 . . .	42
3.14	BELLHOP simulated channel impulse response delay profiles. (left: summer dusk, middle: summer night, right: winter)	42
3.15	Case Study 3.2 weather information and communication performances (Row 1: Air temperature and solar radiation; Row 2: Wind speed and precipitation rate; Row 3: Packet loss ratio and packet header PSNR; Row 4: data block BER. Left column: Rainy and cloudy days 1; middle column: Rainy and cloudy days 2; Right column: Winter windy days)	43
3.16	Case Study 3.1 Histogram of delay of significant peaks at Node C and main tap gain distribution	44
3.17	Case Study 3.2 Histogram of delay of significant peaks at Node C and main tap gain distribution	44
3.18	Air temperature and solar radiation	46
3.19	Wind speed and precipitation rate	46
3.20	Packet loss ratio and PSNR of packet header	46
3.21	BER during flooding	46

3.22	PSNR and packet loss ratio at Node B	47
3.23	BER at Node B	47
3.24	Delay distribution of significant peaks	47
3.25	Histogram fit of the strongest peak	47
4.1	Conditional generative model for UWA CIR	55
4.2	Batch losses during training	58
4.3	Generated samples during training	59
4.4	Amplitude histogram comparison examples (Row 1: Pixel 27, 28, 29; Row 2: Pixel 35, 36, 37)	61
4.5	Power-weighted JSDs calculation (Left: amplitude histogram example of Pixel 32; Right: mean amplitudes of all 256 pixels for this time window)	63
4.6	Power-weighted JSDs of the WCGAN, CGAN, and fitted Rayleigh dis- tribution	63
4.7	Generated CIR samples by varying each Θ value Example 1	64
4.8	Generated CIR samples by varying each Θ value Example 2	65
4.9	Generated CIR samples by varying each Θ value Example 3	65
5.1	Conditional generative model for UWA CIR prediction	72
5.2	Left: original MLP fully connected generator. Right: generator with residual network structure	73
5.3	Batch losses during training	76

5.4	Generated samples during training	78
5.5	Power-weighted JSD of predictions in sunny day time windows . . .	79
5.6	Power-weighted JSD of predictions in cloudy day time windows . .	80
5.7	Power-weighted JSD of predictions in winter day time windows . . .	80
5.8	Histogram of power-weighted JSDs of the predictions, WCGAN generated, and fitted Rayleigh distribution	82

List of Tables

1.1	The published UWA experiment data sets	8
3.1	Number of transmitted packets and obtained CIR samples	30
3.2	JSDs of the four distributions in Figure 3.5	35
4.1	Summary of the WCGAN generator network	56
4.2	Summary of the WCGAN discriminator network	56
4.3	Mean power-weighted JSD of the WCGAN, CGAN, and Rayleigh fitting	63
5.1	Summary of the prediction CGAN generator network	73
5.2	Summary of the prediction CGAN discriminator network	74
5.3	Mean power-weighted JSDs of the predictions for different cases	81

Acknowledgments

Firstly, I would like to thank my advisor, Dr. Zhaohui Wang, for all the patient guidance, support, and consultations for my research.

I am also grateful to my committee members, Dr. Laura E. Brow, Dr. Xiaoyong Yuan, and Dr. Jianhui Yue, for their willingness to challenge my thoughts toward the possible explorations of the subject I discussed in this dissertation.

The field experiments, which collected a significant amount of data that can benefit the research community, were accomplished with the support of the Great Lakes Research Center of Michigan Technological University and the H&Y Marina. I also thank my lab-mate Cheng Fan for his contributions during the experiments.

This dissertation would not have been completed without the help of my uncle Dong Xiang, as well as his friends Tao Hu and Dr. Chuanxiong Guo. The discussions with them not only helped me solve many detailed technical problems but also inspired the outline of this dissertation.

Last but not least, the encouragement from my parents and Prof. Mario Gerla is the reason why I always decided to keep it up when thousands of times that all kinds of anxieties brought up the idea of quitting.

List of Abbreviations

BER	Bit Error Rate
CGAN	Conditional Generative Adversarial Nets
CIR	Channel Impulse Response
CSI	Channel State Information
CTD	Conductivity, Temperature, and Depth
DL	Deep Learning
GAN	Generative Adversarial Networks
JSD	Jensen-Shannon Divergence
KLD	Kullback-Leibler Divergence
MAC	Media Access Control
MI	Magnetic Inductive
OFDM	Orthogonal Frequency-Division Multiplexing
RF	Radio Frequency
SDN	Software-Defined Networking
SER	Symbol Error Rate
SSP	Sound Speed Profile
UWA	Underwater Acoustic
VAE	Variational Auto-Encoder

Abstract

The recent emerging applications of novel underwater systems lead to increasing demand for underwater acoustic (UWA) communication and networking techniques. However, due to the challenging UWA channel characteristics, conventional wireless techniques are rarely applicable to UWA communication and networking. The cognitive and software-defined communication and networking are considered promising architecture of a novel UWA system design. As an essential component of a cognitive communication system, the modeling and prediction of the UWA channel impulse response (CIR) with deep generative models are studied in this work.

Firstly, an underwater acoustic communication and networking testbed is developed for conducting various simulations and field experiments. The proposed test-bed also demonstrated the capabilities of developing and testing SDN protocols for a UWA network in both simulation and field experiments.

Secondly, due to the lack of appropriate UWA CIR data sets for deep learning, a series of field UWA channel experiments have been conducted across a shallow freshwater river. Abundant UWA CIR data under various weather conditions have been collected and studied. The environmental factors that significantly affect the UWA channel state, including the solar radiation rate, the air temperature, the ice cover,

the precipitation rate, etc., are analyzed in the case studies. The obtained UWA CIR data set with significant correlations to weather conditions can benefit future deep-learning research on UWA channels.

Thirdly, a Wasserstein conditional generative adversarial network (WCGAN) is proposed to model the observed UWA CIR distribution. A power-weighted Jensen-Shannon divergence (JSD) is proposed to measure the similarity between the generated distribution and the experimental observations. The CIR samples generated by the WCGAN model show a lower power-weighted JSD than conventional estimated stochastic distributions.

Finally, a modified conditional generative adversarial network (CGAN) model is proposed for predicting the UWA CIR distribution in the 15-minute range near future. This prediction model takes a sequence of historical and forecast weather information with a recent CIR observation as the conditional input. The generated CIR sample predictions also show a lower power-weighted JSD than conventional estimated stochastic distributions.

Chapter 1

Introduction

There are a variety of novel underwater infrastructures that have recently emerged, such as offshore wind generators, deep-sea aquaculture facilities, underwater data center systems, offshore drilling platforms with the subsea oil tree, etc. With the help of advancing robotic and sensing technologies, an accelerated growing number of underwater mobile systems are employed for the construction, deployment, inspection, and maintenance of these underwater infrastructures. The underwater wireless communication and networking system plays an increasingly important part in controlling, coordinating, and cooperating with these underwater mobile systems. However, the underwater wireless communication and networking demands not only still have not yet been satisfied but also are growing rapidly.

The wireless communication paradigms that can be used for underwater mobile systems include underwater magnetic inductive (MI) communication, underwater radio frequency (RF) wireless communication, underwater optical communication, and underwater acoustic (UWA) communication. Both the underwater MI and RF support \sim Mbps level high data rate, but their communication ranges are within \sim 10m due to the absorption of electrical magnetic waves by the water, especially the seawater. The underwater optical communication also supports a high data rate within the \sim 100m range due to obstacles, light scattering, and ambient light noises. The UWA communication supports \sim kbps data rate within the \sim 10km range and has been playing an important role in wireless communication and networking of underwater systems. Given the operating range and environment of underwater infrastructures with mobile systems, UWA communication is considered the only practical paradigm with balanced power efficiency, data rate, and communication range for underwater networks.

Due to the distinctive physical characteristics of sound propagation in water, the UWA channel is considered one of the most challenging wireless communication channels that are different from the well-studied and standardized terrestrial RF channels [2, 3, 4]. Sound propagation speed in water is about 1500 m/s, which is much slower than the RF waveform speed. Thus, the UWA channel has a significant propagation delay. Moreover, the sound speed is usually inhomogeneously distributed at

different depths because the underwater sound speed depends on the salinity/Conductivity, Temperature, and pressure/Depth (CTD) of the water. According to the inhomogeneous distribution of speed, underwater acoustic rays converge and diverge at different locations under complex refraction conditions. Combined with the reflections of sound waves at the surface and the bottom, the multi-path of the UWA channel is more complex due to the propagation ray distributions. Depending on the multi-path geometry and the sound speed profile, the delay spread of a UWA channel can be as long as $\sim 100\text{ms}$ [5], which is in the same order as a data frame duration. The underwater acoustic attenuation consists of both spreading loss and absorption loss, which lead to acoustic signal traveling along a path with a longer distance that may have a shorter propagation delay but a more extensive path loss [2]. Since the UWA attenuation is frequency-dependent and the signal with a higher frequency has a higher absorption rate, the available bandwidth for UWA communication is minimal and usually in the same order as the center frequency [2]. Hence, the narrow-band assumptions typically used in RF communication rarely apply to UWA channels [3, 6, 7]. As the attenuation of UWA waveform increases with frequency, the available bandwidth could be extremely limited but not negligible with respect to the center frequency, which causes that UWA communication systems are inherently wide-band and the achievable data rates heavily depend on the distance.[2] For example, 50 bit/s was achieved over $\sim 550\text{ km}$ in [8], while, in offshore shallow water, $\sim 5\text{ Kbit/s}$ could be achieved over $\sim 5\text{ km}$ [9], and $\sim 1\text{ Mbit/s}$ was achieved

over 100 m in a small lake [10]. The Doppler spreading and shifting of UWA is much more significant in RF communication since the speed of sound in water is only about 1500 m/s, and many mobile platforms can operate at 10 m/s or faster. Even if transmitters and receivers were stationary, path-specific Doppler rates were often observed in field experiments due to the dynamics introduced by currents and waves [7]. In addition to the ambient noises caused by tides, currents, storms, wind, rain, etc., the UWA communication bandwidth also overlaps with the spectrum used by some sea creatures and the mechanical noises caused by other artificial system activities [11].

The variations in these UWA channel characteristics also show significant spatial-temporal correlations [12]. Besides the movement of the transmitters and receivers, most of the environmental factors that influence the UWA channel characteristics are mainly related to variations from two perspectives, namely the sound interactions with the surface or bottom and the inhomogeneity of the water medium [13]. The localized geographic features, such as the bottom's topography and sediment components, strongly affect the sound ray tracing spreading patterns from the bottom reflection perspective. In addition, temporal variational factors, such as the weather conditions and the hydrodynamic movements of the water body, affect the UWA channel characteristics by agitating the surface reflections and fluctuating the inhomogeneity of the underwater CTD distribution. These spatial-temporal variational factors result in UWA channels observed in different field experiments often follow distinct patterns [4]. The relatively static spatial and long-term temporal correlated

variations of a UWA channel result in localized deterministic characters of the UWA channel patterns, such as the nominal acoustic propagation that could be analyzed by ray tracing models. Other short-term temporal correlated variations affect the uncertainty patterns of a UWA channel under different conditions. These short-term variations were conventionally modeled by stochastic distributions.

UWA communication and networking techniques require specialized designs to handle the challenging UWA channel characteristics, including but not limited to the large propagation delay, limited available bandwidth, high error probability, etc [14]. The conventional RF wireless communication techniques rarely show satisfying performances when tackling these challenging characteristics of UWA channels by only tuning timings and adjusting parameters [4]. To develop a UWA application-optimized communication and networking system, the resource-aware and constraint-aware cognitive design is the key to addressing the challenging UWA channel characteristics in real-time.

The workflow of a typical cognitive communication system is shown in Figure 1.1 [1]. The cognitive communication system concurrently monitors the environment and acquires an awareness of the channel state information (CSI) based on its knowledge database. With a prediction of possible states, the cognitive communication system will infer the performances of available communication configuration options. An optimal communication configuration will be decided based on performance predictions

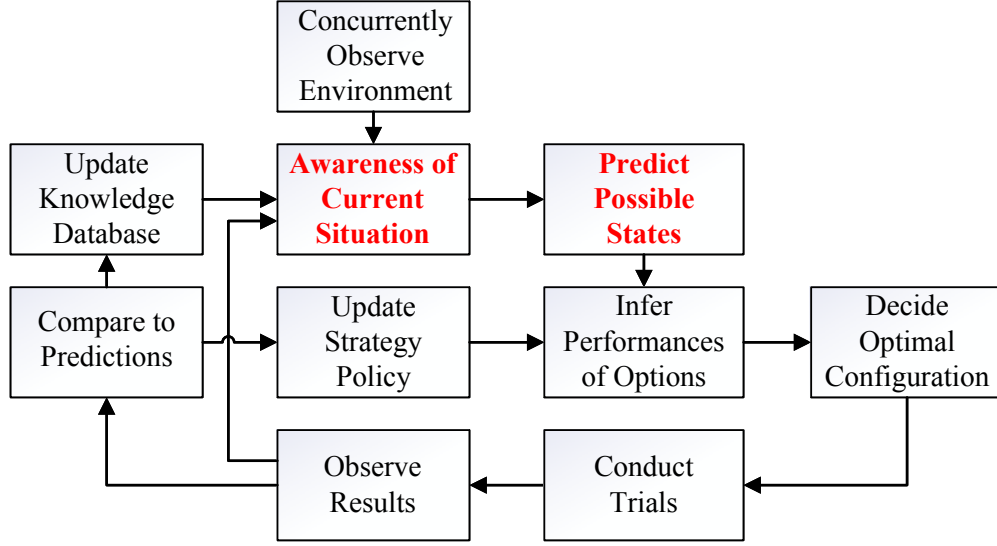


Figure 1.1: The workflow of a cognitive communication system [1]

and communication strategies. After conducting a series of communication trials, the communication results will be collected to compare to the previous predictions. Then, the knowledge database for CSI awareness modeling and prediction will be updated based on the differences between the communication results and the predictions, as well as the communication strategy policies.

Due to the uncertainty of communication media, the CSI usually can be considered random variables following stochastic distributions, which are conditioned on the environment states. Hence, the optimal configuration is decided based on the performance expectation of a specific communication option over the distribution of the random CSI. This performance expectation can be estimated by directly averaging the results of multiple communication trials due to the short delays and low power consumption of RF communications. However, effective estimations cannot be obtained in time

due to the long delays, the high error rate, and the fast-fading characteristics of UWA channels. Moreover, the limited battery capacity of the underwater system also cannot afford the high transmission power consumption of frequent UWA communication trials. Thus, UWA channel modeling and simulations play an essential part in the cognitive UWA communication system.

In practical communication scenarios, the CSI can be modeled as a channel impulse response (CIR) function and formulated as:

$$h(t) = \sum_{p=1}^{N_p} A_p \delta(t - \tau_p) e^{2\pi j \theta_p} \quad (1.1)$$

where N_p denotes the total number of multi-paths. A_p , τ_p , and θ_p denote the gain, delay, and phase shift of the p th path, respectively. In conventional RF communication theory assumptions, A_p follows distributions such as Rayleigh distribution, Rician distribution, Log-Normal distribution, or Nakagami distribution for different simplified channel types. τ_p can be assumed following exponential distributions. However, due to the challenging UWA channel characteristics, there is no standardized categorization of UWA channel types [4]. The long delay spread and complex multi-path conditions lead to an elusive mathematical description of the UWA CIR function. The conventional distribution parameter estimation methods used for RF channels may no longer be applicable for UWA channels [2].

Meanwhile, similar challenges are encountered by machine learning models when trying to model a picture by the joint probability distribution of values at each pixel. The deep generative models show impressive performance for representing the distribution of pixel values of a picture [15]. A deep generative model can learn the target distribution of a picture. Then, the trained deep generative model can convert random samples drawn from a known standard distribution, i.e., the standard Normal distribution, to values following the learned target distribution of the pictures. If a deep generative model can learn the distribution of UWA channels, the generated samples can be used to evaluate the performances of configuration options under different conditions.

Table 1.1
The published UWA experiment data sets

Data set	TX interval	Available CIR samples	Maximum compatible CIR samples
SPACE 08[16]	2 hours	781440	56880
MACE 10[17]	4 min	46128	23808
Watermark[18]	6-10 min	56664	30600
KWAUG14[12]	15 min	34640	34640

Much research has been carried out on using machine learning for adaptive UWA communication in recent years [19, 20, 21, 22]. In an ideal case, a large amount of UWA CIR data for training and evaluating these machine learning models should be generated by UWA channel simulators. However, existing UWA channel simulators can usually only simulate certain aspects of the channel. A few UWA channel models

have demonstrated the capability to simulate the CIRs that match the data on a time scale appropriate for practical adaptive communication scenarios [4, 13]. Even if such a simulator exists, it is difficult to provide sufficient detailed data on environmental factors, especially their temporal variations, for a realistic simulation. Thus, the field experiment data still play an essential part in the analysis and evaluation of UWA communication designs [4, 13]. The CIR observations from field experiments can be stochastically replayed with random noise to simulate a UWA channel. An ensemble of CIR observations from multiple field experiments was collected as a benchmark for UWA physical layer algorithms [18]. In [13], a database of ocean CIR was proposed, and the characteristics of interests for the UWA channel were pointed out to ensure the validity and reusability of the UWA channel data for UWA communication performance evaluation purposes. However, besides the CIR data itself, the real-time environmental data, such as the air temperature, wind, rain, etc., can also be utilized for predicting the UWA channel state, thereby contributing to the optimal adaptive UWA communication scheme selection. Due to the high costs of UWA communication experiments, as shown in Table 1.1, there is no available published UWA data set with sufficient CIR samples for training a deep learning model. Since the objectives of these experiments were not targeting estimating the CIR distribution, the transmission intervals between packets were designed as long as tens of minutes to extend the battery lifetime of the deployed system. Hence, there are only tens of CIR samples can be used to estimate an instantaneous channel state.

This thesis mainly focuses on employing deep learning models to contribute to the awareness of the current situation and predict possible states as part of a cognitive communication system. A test-bed system has been developed for conducting field UWA communication experiments to collect the CIR samples for training deep learning models. With the help of the proposed test-bed system, a series of field experiments have been conducted in a shallow freshwater area across a river under various weather conditions in different seasons. Abundant UWA CIR data has been collected with corresponding real-time weather information. The characteristics of the UWA channel impulse response distribution are analyzed in the case studies of the field experiment data. To model the various UWA channel distribution patterns under different weather conditions, a Wasserstein conditional generative adversarial network (WCGAN) is proposed to learn the representation of the UWA CIR distributions. Then, a modified conditional generative adversarial network (CGAN) taking weather data sequences as input is proposed to perform the channel state prediction.

This dissertation mainly consists of four parts:

First, the UWA test-bed system developed for simulation and field experiments is introduced in Chapter 2. Nodes equipped with UWA modems can be deployed in the field environment and remotely controlled during the experiment. The UWA network protocols can be developed and tested in the simulation environment. Then the program can be directly migrated to emulation and field experiment systems for

real-environment experiments.

Second, in Chapter 3, a field experiment across the Keweenaw Waterway was conducted to collect the UWA channel state information data. Abundant UWA CIR samples under various weather conditions were collected for training deep learning models. The temperature and solar radiation rate that affect the water temperature distribution at different depths showed significant correlations to the UWA communication performances. The precipitation and wind speed also affect the signal-to-noise ratio of the received UWA waveform.

Third, a WCGAN is proposed to model the UWA CIR distribution in Chapter 4. A power-weighted JensenShannon divergence (JSD) is proposed to measure the similarity between the generated distribution and the experimental observations. The CIR samples generated by the WCGAN model show a lower power-weighted JSD than conventional estimated stochastic distributions.

Fourth, in Chapter 5, a modified CGAN model is proposed for predicting the UWA CIR distribution in the 15-minute-range near future. This prediction model takes a sequence of historical and forecast weather information with a recent CIR observation as the conditional input. The generated CIR sample predictions also show a lower power-weighted JSD than conventional estimated stochastic distributions.

Chapter 2

An Experiment Test-bed for Underwater Acoustic Communication and Networking

A UWA test-bed is designed to conduct multiple UWA communication and networking experiments in various environments, including simulation, in-lab emulation, and field experiments. A UWA test-bed for field experiments usually consists of an on-shore control center, several surface nodes equipped with both RF and UWA modems, and sometimes UWA bottom nodes or underwater mobile nodes. The control center provides a web user interface for operating the equipment, uploading programs, and downloading experiment data. A user can send commands to operate the surface

nodes deployed in the field via RF link from the control center to run the UWA communication or networking experiment programs. Due to the high deployment costs and limited system battery lifetime in the field environment, the simulation and in-lab emulation systems play an essential part in developing and testing the hardware and software systems for a UWA field experiment.

The objective of developing this test-bed system includes collecting UWA CIR data with corresponding environmental data under different weather conditions for deep learning. Thus, field node deployment time lasts at least several days are expected. The local data storage space and the battery lifetime of field nodes must be tailored for such deployment duration. The various weather conditions during deployment also require the electronic devices of field nodes must be hosted with water-proof and weather-proof enclosures. Moreover, the environmental sensors collecting corresponding weather data are also needed.

This chapter introduced the hardware system design of the test-bed and summarized the experiments facilitated by this test-bed.

Part of this chapter was published at the 16th International Conference on Underwater Networks & Systems (WUWNet22), November, 14-16, 2022, Boston [23] (<https://doi.org/10.1145/3567600.3568155>).

2.1 Related work on UWA test-bed system

In [24], most of the popular UWA communication and networking test-beds are reviewed and compared in detail from both the hardware and software system perspectives, including DESERT [25], SUNSET [26], Ocean-TUNE [9], and SUNRISE [27]. Most field experiment systems employ a host device running an operating system to control the acoustic modems. By remotely accessing the host device, one can perform UWA communication or networking experiments by running a script or program in the host operating system. The remote access and control of the host device can be implemented via WiFi, RF modems, cellular modems, or acoustic modems.

The field experiment test-beds can be categorized as long-term and short-term, and high-cost and low-cost designs. The long-term design is usually for experiments that require multiple field trips to deploy and recover nodes. The long-term surface nodes are usually equipped with a heavy battery pack and solar panels mounted on a large buoy that needs a crane to deploy [28]. Even if equipped with solar panels, the on-duty time of the test-beds mentioned above is still constrained by the battery lifetime of their system. In contrast, short-term experiments are often finished within a single field trip. The light-weighted platform of short-term test-beds only needs water-proof enclosures to prevent short circuits. The weather-proof design for long-term design may be optional. Although there are cabled offshore test-beds such as the Ocean

Observatories Initiative (OOI) [29] that can support long-term deployment without battery lifetime constraints, the data obtained in UWA communication-related experiments are usually processed offline after the devices are recovered. Because most commercial acoustic modems still use RS232/485 serial ports to communicate with host devices, the received waveform is usually too large to transmit back in real-time during a deployment. Thus, the OOI test-bed is better utilized by oceanographic researchers to collect measurements of various environmental data.

2.2 Test-bed system design

The hardware system consists of a control center, a RF master node, multiple field nodes, and environmental data sensors including a weather station and the web cameras monitoring the surrounding area. The schematic diagram of the experiment system is shown in Fig. 2.1.

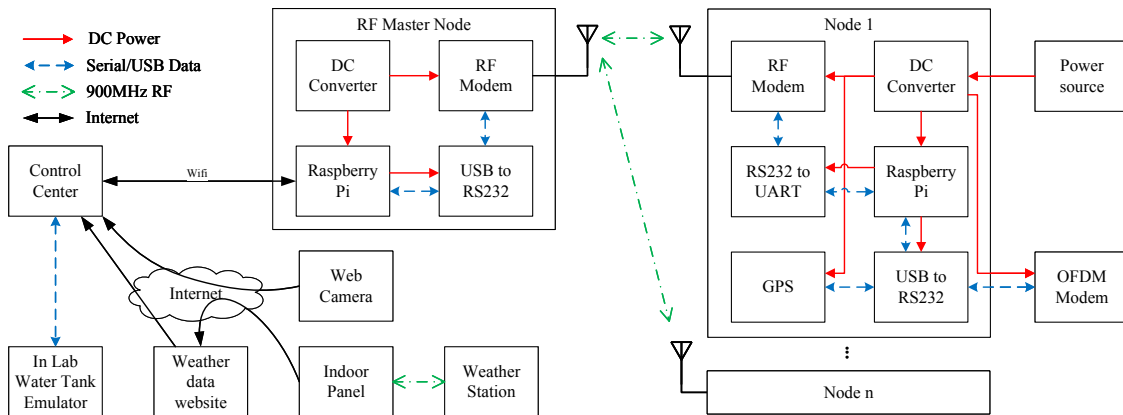


Figure 2.1: Schematic diagram of the experiment system

The field node employed in this experiment is a low-cost design version of the Ocean-TUNE[9] test-bed surface nodes, which integrate commercial devices. A field node consists of a control box, an AquaSeNT AM-OFDM-13A acoustic modem, and a power source. As shown in Fig. 2.2, a control box hosts a Raspberry Pi as the host device, a MicroHard n920 RF modem for remote control, a GPS, two different serial port converters, and two DC-DC converters providing 12V and 5V DC power supply. In different situations, the Raspberry Pi can be remotely accessed via the on-board WiFi module, the RF modem connecting to the console port, or the acoustic modem with SeaLinx[30] acoustic remote control module running. The housing of the field node should be both submersible and weatherproof. A sizeable diurnal amplitude can cause condensation inside the box, and the accumulated dew may cause short circuits of electronic devices. To avoid cumulative condensation, rather than cable glands, waterproof penetration connectors with bulkheads are preferred for connecting the control box with other equipment. The box should avoid having clear windows on the top. All the electronic devices should be mounted on an elevated panel, and wires should be appropriately connected and organized. Some desiccant packs could be kept in the box during the deployment time.

Since the RF modems are working in a master-slave mode, there is an RF master node that works as the gateway node connecting the control center and all field nodes. The RF master node was deployed inside the building, which is within the WiFi coverage and can overlook all field nodes. By remote accessing the Raspberry

Pi of the RF master node, one can use serial port terminal programs like Minicom to type commands, operate the master RF modem, and communicate with Raspberry Pis in each field node control box.

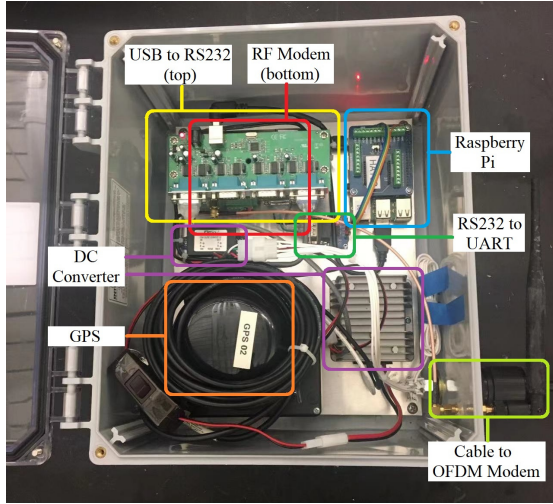


Figure 2.2: Field node control box



Figure 2.3: Weather station sensor

As shown in Fig. 2.3, the Sainlogic FT0835-plus weather station used in this experiment is a smart home device that costs less than two hundred dollars. The outdoor weather station sensor first reports data samples to an indoor control panel via a 900MHz RF link. Then, the indoor control panel will upload the weather data to a weather data website once every minute. The 5-minute average weather data will be recorded on the website, including historical data from all other available weather stations in the neighborhood. A python crawler script was developed to collect a weather station data sample and a screen-shot of the public web camera from corresponding websites every minute. Moreover, the web camera monitoring the campus area can also be hooked up in the test-bed and provide pictures of some experiment

area every minute.

The emulation system of the test-bed consists of lab UWA modems directly connected to the control center server via serial ports. The field nodes can be tested with the lab UWA modems in a water tank before the field deployment trip.

2.3 UWA channel test capability

The UWA channel tests usually transmit the designed UWA waveform from one or multiple sender nodes and then collect the received waveform at the other receiver nodes. The proposed test-bed has supported UWA channel tests collecting UWA channel data for multiple research projects at different locations under various weather conditions. In [31], a field node was integrated with an unmanned surface vehicle and collected UWA channel data from the mobile node. In [32], seven field nodes were deployed in the Keweenaw Waterway area to study the spatial-temporal variations of the UWA channel in both summer and winter time. The proposed test-bed field nodes also supported the under-ice UWA channel experiments in Portage Lake.

2.4 UWA networking test capability

Besides the aforementioned UWA communication experiments, the proposed test-bed also supports multiple types of UWA networking experiments. In [33], a software-defined networking (SDN) simulation experiment was conducted by integrating the mininet [34] platform with UWA channels simulated by ns-3 [35]. The simulated UWA SDN was configured and operated with the OpenFlow protocol [36]. A UWA media access control (MAC) protocol was developed with the SDN platform of this test-bed in [37, 38]. The developed UWA SDN MAC protocol was tested in simulation, emulation, and field experiments hosted by the proposed test-bed [38].

2.5 Summary of the test-bed system

The test-bed is a low-cost design for long-term UWA field experiments. The submersible and weather-proof field node design with the UWA modem memory space extension fulfilled the long-term intensive UWA channel experiment requirements. The proposed test-bed system demonstrated its capabilities of hosting the UWA communication experiment in multiple research projects, as well as the simulation, emulation, and field experiments of UWA SDN tests.

Chapter 3

An Experimental Study of Underwater Acoustic Channel Impulse Response Distributions in the Keweenaw Waterway

The typical UWA channel experiments are simply transmitting and receiving UWA waveforms designed for UWA communication. Usually, the transmitted waveform is designed based on signal processing algorithms to be evaluated in the experiment. The UWA CIR can be estimated by comparing the transmitted and received waveform. The monitored ambient noise and observed CIR can be used for stochastic replay

modeling of the UWA channel in simulation experiments. Also, the signal level communication performance metrics, such as signal-to-noise ratio (SNR), Doppler effect, and bit error rate (BER), can be used as references for setting parameters in UWA communication and networking simulations. Since only the frequency band utilized by the transmitted waveform can be studied, the design of the waveform and transmission patterns determines how the UWA channel characteristics can be observed from the received data.

The objective of conducting this experiment is to collect abundant data for modeling the UWA channel with deep learning models. The UWA CIR data is supposed to be sampled as frequently as possible to illustrate the instantaneous distribution of the UWA channel. Meanwhile, the duration of the waveform transmission should also be continuous and as long as possible for studying both small-scale and large-scale variations of the UWA channel.

This chapter presents an experimental study of UWA CIRs in the Keweenaw Waterway. An orthogonal frequency division multiplexing (OFDM) waveform was intensively transmitted at the same location for several days in different seasons. The abundantly received signal was collected with real-time weather information. The temperature, solar radiation, wind speed, and precipitation are observed as the primary weather factors that influence the UWA channel. The obtained data has been

organized as the first UWA channel database consisting of millions of CIR data samples and corresponding real-time weather information at a minute-level sampling rate, which could facilitate future machine learning research of UWA communication. The CIR data shows obvious correlations to some environmental conditions. The UWA CIRs under several typical channel conditions are introduced in detail in the case studies. The phenomena discussed in these case studies can be features of interest for future deep learning models.

Part of this chapter was published at the 16th International Conference on Underwater Networks & Systems (WUWNet22), November, 14-16, 2022, Boston [23] (<https://doi.org/10.1145/3567600.3568155>).

3.1 Related work on the experimental study of UWA channel

The CIR is estimated by processing the received waveform obtained during a UWA communication experiment. Hence, the waveform to be transmitted is usually designed for evaluating proposed signal processing algorithms rather than for collecting a CIR data set. Due to the high costs, most existing field experiments transmit waveform either intensively in a burst for short-term tests or periodically once every tens of minutes for long-term tests. The CIRs obtained in either experiment scheduling

can usually only reflect small-scale or large-scale variations, but rarely both.

In short-term experiments that deploy and recover the equipment during the same voyage, a common experiment design is to transmit the designed waveform in a burst of several hundreds of packets or data frames, i.e. in [39, 40]. The intensive transmission schedule is targeting obtaining sufficient data samples to demonstrate the effectiveness of the studied algorithms. Besides leaving the equipment in water overnight may not be allowed in the shallow water area, the field nodes qualified for overnight deployment are expensive due to the mooring size requirement and the extra devices for traffic safety concerns. Considering the high costs of ship voyages to the offshore area, the intense transmitting scheduling is preferred for minimizing the total deployment time. The short-term intense transmitting scheduling can better help observe small-scale variations due to more CIR samples in a short time period being obtained, but the large-scale variations that span in periods of hours or days may not be able to be observed during the short total deployment time.

In long-term experiments that recover the deployed equipment in a second voyage, the waveform is usually periodically transmitted in a frequency as low as once every 15-60 minutes, i.e. the SPACE08 and MACE10 experiments in [41] or the KWAUG14 experiment in [12]. The periodical transmission schedule can obtain diverse data samples at different times of a day. The long idle time between transmissions can extend the total battery lifetime by utilizing the recovery effect of the battery, and

transmitting in a burst will drain the battery faster due to the battery rate capacity effect [9].

According to existing field experiment data, neither of these two experiment designs can obtain a decent histogram of the UWA CIRs that can illustrate both the small-scale and large-scale variations, especially for studying the spatial-temporal correlations of UWA CIRs and the environment data.

3.2 Experiment Design

The experiment design of a UWA channel experiment includes the design of the waveform and the transmission procedure. The waveform design is based on the signal processing algorithms used for estimating the UWA channel, which determines what channel characteristics can be observed from the experiment data. The transmission procedure determined the CIR sampling rate and experiment duration. The CIR sampling rate determines how well the instantaneous CIR distribution can be estimated. The experiment duration should be sufficient for reflecting the large-scale variations of the UWA channel.

3.2.1 Transmitted OFDM Waveform

As shown in Fig. 3.1, the transmitted waveform consists of several preambles, 20 ZP-OFDM [42] data blocks, a one-second idle time for recording the background noise, and an ending Hyperbolic Frequency Modulation (HFM) chirp. The total duration of the waveform is about 9s, but when it is transmitted by the AquaSeNT OFDM modem, an extra preamble will be added to the waveform. If the modem-added preamble is not detected or correctly decoded, the waveform will not be recorded by the receiving UWA modem.

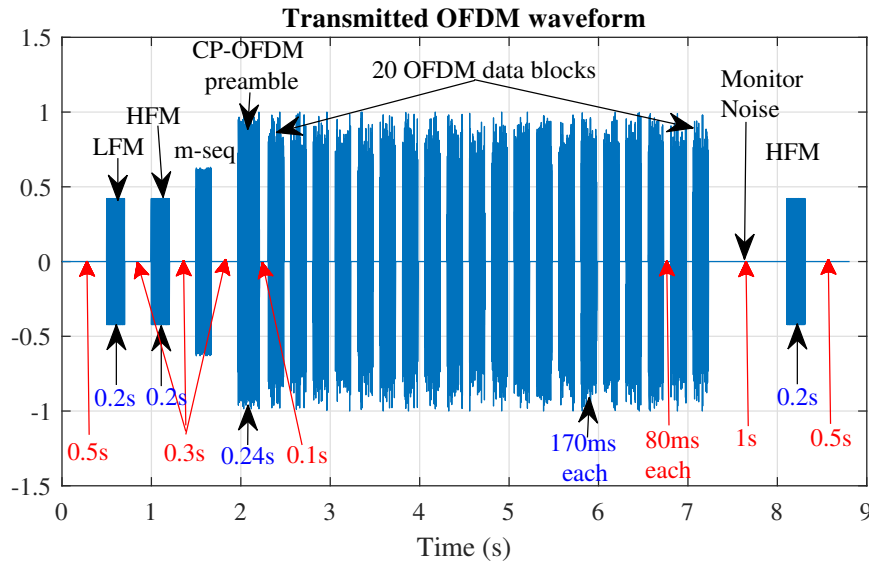


Figure 3.1: The transmitted OFDM waveform

The transmitted waveform uses the 21-27kHz frequency band. For the OFDM data blocks, there are 1024 subcarriers uniformly allocated in the 6kHz bandwidth, which consists of 256 pilot subcarriers, 672 data subcarriers, and 96 null subcarriers. The 256

pilot subcarriers are evenly located at the $(4k - 1)$ th subcarriers, $k = 1, 2, 3, \dots, 256$. Besides the one pilot subcarrier in every 4 adjacent subcarriers, the lowest and highest 32 subcarriers are filled with null subcarriers. All data subcarriers are located in the middle frequency range, and there is one null subcarrier in every 20 adjacent subcarriers among the data subcarriers. Each data block lasts 170ms and is followed by an 80ms guard time interval. In a conventional communication scenario, the signal at pilot subcarriers is known to be both the sender and the receiver. The CIR can be estimated based on the received signal at the pilot subcarriers. Then, the data symbols can be detected based on the estimated CIR.

3.2.2 Experiment transmission Procedure

There was one transmitter and two receivers during three deployment stages. The deployment locations are shown in Fig. 3.2. The transmitter was deployed at Node A. The two receivers were deployed at Node B and Node C during the first two deployments and then changed to Node C and Node D during the third deployment due to location availability issues. The distance between Node A and B is about 300 meters, and the distance from Node A to Node C or D is about 600 meters. Each receiver node was equipped with two acoustic modems with different hardware configurations. The acoustic modems were deployed at the depths around half of the water depths at their deployment locations.

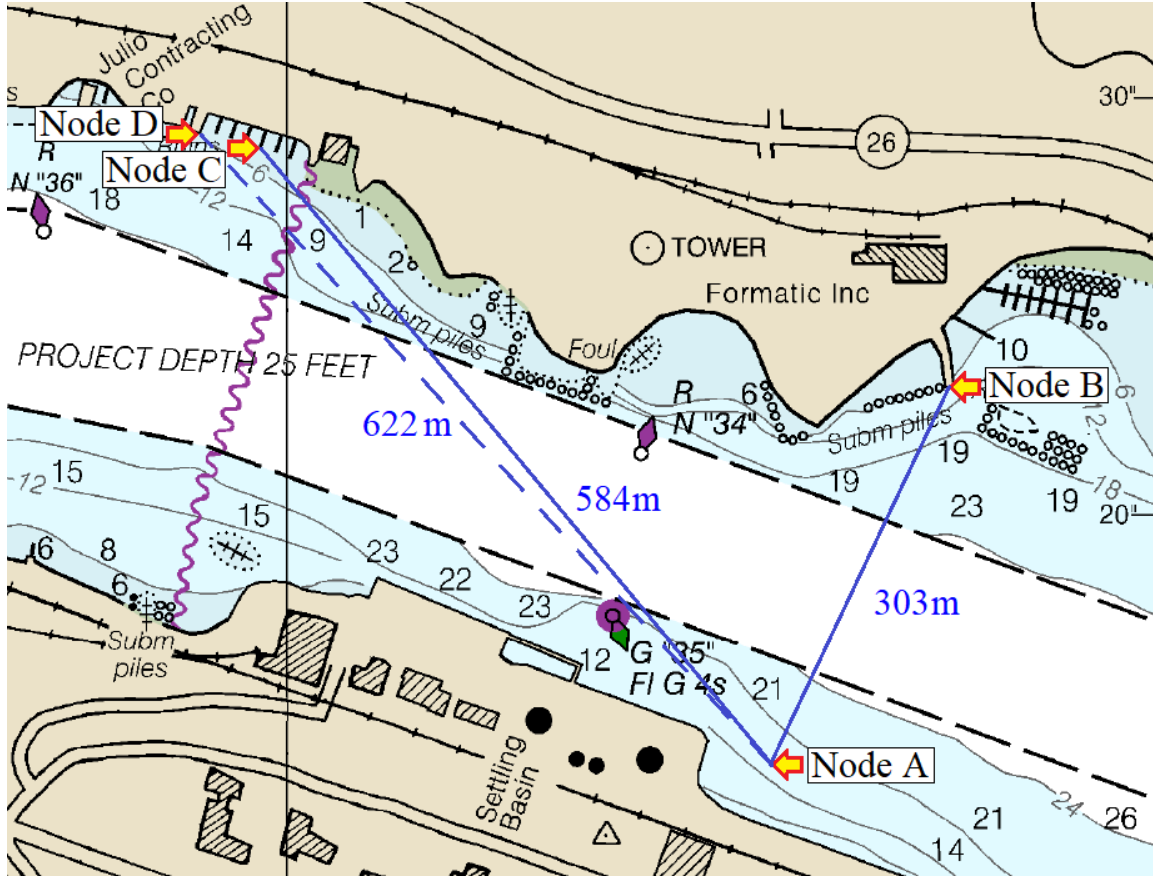


Figure 3.2: Deployment locations of the acoustic modems

The OFDM waveform and a short text message were transmitted during the experiment every 20s. Meanwhile, the weather station mounted at Node A, as shown in Figure 2.3, reports the weather data every minute to a weather data website. A web crawler program running on the control center can log these 1-minute data with a permitted API. The website also logged the 5-minute average of the weather data of all weather stations nearby. The campus webcams monitoring the experiment area provide a bird-view of the river surface. The screenshot of these webcams can be recorded every minute with a web crawler program. There is also a time-lapse file for each day available on the webcam website. Screenshots of every 5 minutes can be

extracted from the time-lapse file.

3.3 Field Experiment Results and analysis

There were three deployment stages started on 12/22/2021, 04/19/2022, and 05/18/2022. The experiments were interrupted several times due to various reasons. Thus, there are seven effective experiment stages as listed in Table 3.1.

3.3.1 Data obtained

There are three types of data obtained from the presented experiments, namely the environmental data, the communication performance measures obtained from decoding the packet headers, and the channel information from processing the received waveform. All these data are organized with the timestamp and equipment ID information in a MySQL database.

The weather data from the weather stations include the temperature, dew point, humidity, wind speed, wind gust, pressure, precipitation rate, solar radiation rate, etc.

The OFDM modem generated a packet header for each OFDM waveform and text

message transmission. By decoding this header, several communication performance measures were provided in the acoustic modem log file, including input signal-to-noise ratio (INSNR), pilot signal-to-noise ratio (PSNR), effective signal-to-noise ratio [43], center frequency offset (CFO), etc. These communication performance measures can be used as references for parameter settings in network simulations.

The received OFDM waveform was stored in the modem only when the packet header had been correctly decoded. There are 4 receiving hydrophones on each acoustic modem, and there are 20 OFDM blocks within each OFDM waveform. Thus, 80 CIR samples can be obtained from a successfully decoded OFDM waveform packet. Except for the lost packets or the waveform that cannot be decoded, the total CIR samples obtained during each deployment are listed in Table 3.1.

Table 3.1
Number of transmitted packets and obtained CIR samples

Start Date	TX pkts	Node B		Node C		Node D	
		M 04	M 47	M 02	M 41	M 04	M 47
12/24/21	19788	1559200	1555520	1571120	1581920	-	-
04/19/22	3400	271840	271840	267280	267600	-	-
04/21/22	29532	2356000	2352960	2358800	2358880	-	-
04/30/22	1166	93120	93200	70800	77760	-	-
05/01/22	4359	348480	348640	275200	330240	-	-
05/19/22	10496	-	-	808080	788560	800640	768640
05/22/22	26587	-	-	1870000	1793680	1787200	1755200
Subtotal	95328	4628640	4622160	7221360	7198560	2587840	2523840
Total CIR						28782400	

3.3.2 Channel Impulse Response Results and Analysis

The CIRs are estimated with the received signal at the frequencies of pilot subcarriers with both least squares (LS) and SpaRSA channel estimator [44]. A CIR sample in its time domain representation is a vector of 256 complex values and a vector of 1024 complex values in its frequency domain representation. The time resolution of these 256 pixels is $1/(2BW) = 1/12\text{ms}$, and the observable channel time is about 21.33ms. Since the start time of the estimated CIR is determined by the synchronization process of the signal, we can shift the CIR array circularly to align the value with the largest amplitude, namely the main tap, to a specific pixel without affecting the decoding accuracy. In our data set, the main taps are aligned to the 30th pixel of the CIR vector.

By grouping the CIRs obtained within a time window, here we briefly reviewed the CIR in the time domain from the arrival time distributions of the multi-paths, as well as the tap gain distributions.

3.3.3 The Arrival Time Distributions of Significant Taps

After aligning the main peak value with the largest amplitude in a time domain CIR sample to the 30th pixel of the 256-value CIR vector, the delay spread distributions

of other paths can be studied by analyzing the relative delay of significant taps to the main peak. As shown in the left figure in Figure 3.3, a significant tap in a CIR sample is a value whose amplitude is larger than both adjacent pixels and 0.05 of the largest amplitude value. By histogram of the arrival time of the 10 largest significant taps, the distribution of significant tap arrival times of a single time window is shown in the middle figure of Figure 3.3. Then, after aligning the histogram of significant tap arrival times for all time windows together, the large-scale variations of the tap arrival time distributions are shown as the time lapse in the right figure of Figure 3.3.

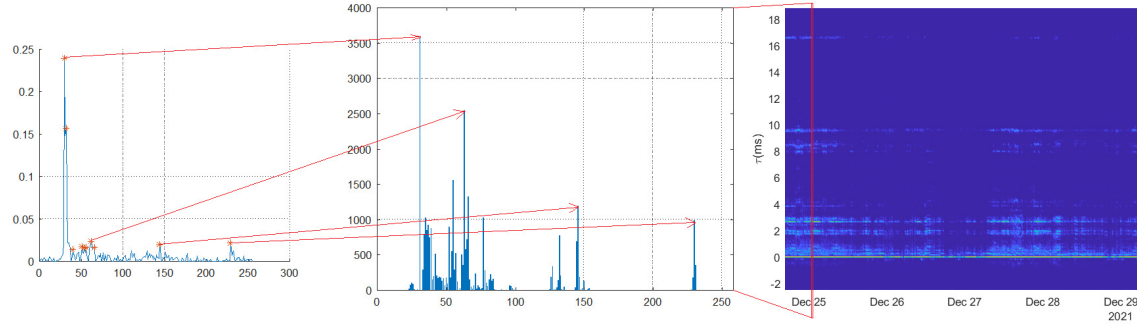


Figure 3.3: Histogram of arrival times of significant taps

3.3.4 The Main Tap Gain Distributions

The main peak amplitude histogram of CIRs within a one-hour time window is shown in Figure 3.4. The amplitude values are fitted to the classic distributions used in RF communication assumptions for tap gain distributions, including the Rayleigh, Rician, Log-Normal, and Nakagami distributions. The parameters of these distributions are

estimated by calculating the corresponding observed CIR values and then converted to an equivalent power mass distribution (PMF) at each histogram bin center as shown in Figure 3.4. Then, the equivalent JensenShannon divergence (JSD) [45] of the observed CIR histogram and each distribution with its estimated parameters can be calculated with the following equation.

$$JSD(P \parallel Q) = \frac{1}{2}KLD(P \parallel M) + \frac{1}{2}KLD(Q \parallel M) \quad (3.1)$$

where M is the average PMF of two distributions

$$M = \frac{1}{2}(P + Q) \quad (3.2)$$

and the $KLD(P \parallel M)$ denotes the KullbackLeibler divergence (KLD) [46]

$$KLD(P \parallel M) = \begin{cases} \sum P(x) \log \left(\frac{P(x)}{M(x)} \right) & , P(x) > 0 \\ 0 & , P(x) = 0 \end{cases} \quad (3.3)$$

The distribution with the lowest JSD value fits the observed CIR histogram the best.

Due to the temporal variations of the UWA channel, the CSI may significantly vary within the histogram time window. Thus, the amplitude histogram of the main peak will no longer satisfy the communication theory assumptions for the four classic distributions. As shown in Figure 3.5, there are multiple peaks can be observed in

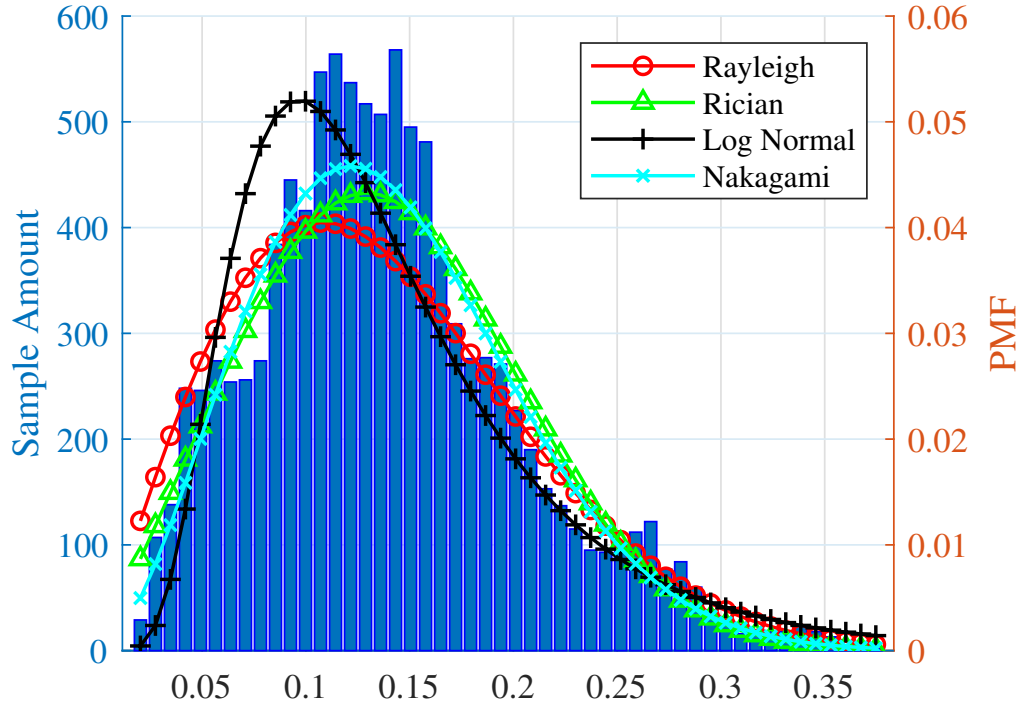


Figure 3.4: An example of the histogram of the main peak gains in a 1-hour time window

the histogram of some time windows, which will result in large JSD values for all four distributions. Also, as listed in Table 3.2, the distribution with the least JSD value may vary for different time windows.

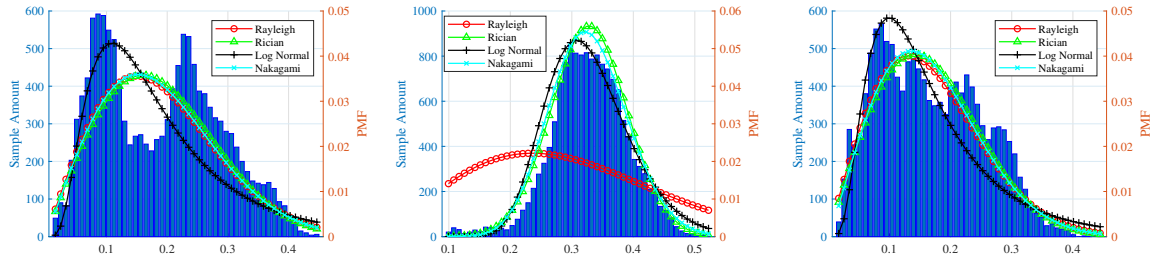


Figure 3.5: Histogram fit examples with different JSD

As shown in 3.6, the JSD of each distribution varies as the time window slides. The

Table 3.2
JSDs of the four distributions in Figure 3.5

Distribution	Left	Middle	Right
Rayleigh	0.0185	0.1238	0.0092
Rician	0.0184	0.0053	0.0086
Log Normal	0.0267	0.0156	0.0207
Nakagami	0.0187	0.0079	0.0092

color of the shadow on the top part of each figure denotes which distribution has the least JSD during each time window.

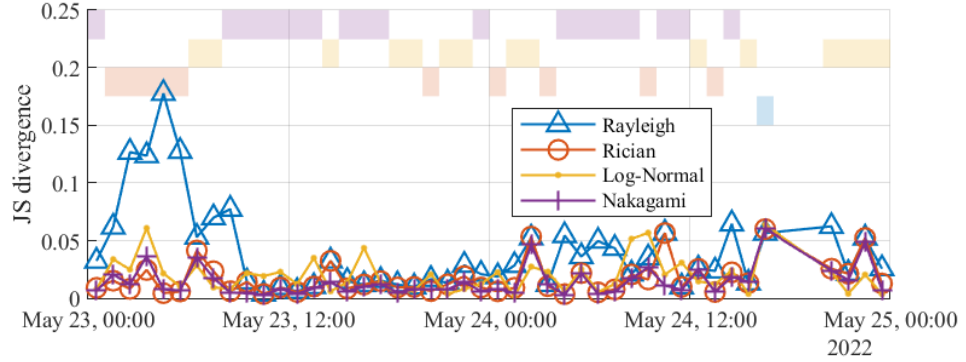


Figure 3.6: An example of the JSD trend

3.4 Case Study 3.1: UWA Channel affected by Water Temperature Distribution

The propagation speed of underwater acoustic waveform is determined by the conductivity, temperature, and depth of the water. Since the experiments were in a shallow freshwater area, the water temperature distribution is the main factor that affects the

sound speed profile (SSP). With an inhomogeneous distributed SSP, the sound ray will travel along a curved ray. The CIRs observed in the experiments show that the water temperature distribution significantly affected the UWA channel.

The UWA CIRs at different weather conditions, which leads to different water temperature distributions, are shown in Figure 3.7 and Figure 3.16. The first row of Figure 3.7 show the air temperature and solar radiation data that affect the water temperature. The second row shows the wind speed and precipitation rate that affects the water surface condition. The third row shows the packet loss ratio and the PSNR range of received packet headers for each 15-minute time window. The blue line is the average PSNR, and the light blue shading area denotes the 90% middle-value range PSNR values. The fourth row shows the average and the 90% middle-value range of the bit error rate (BER) of the received OFDM waveform.

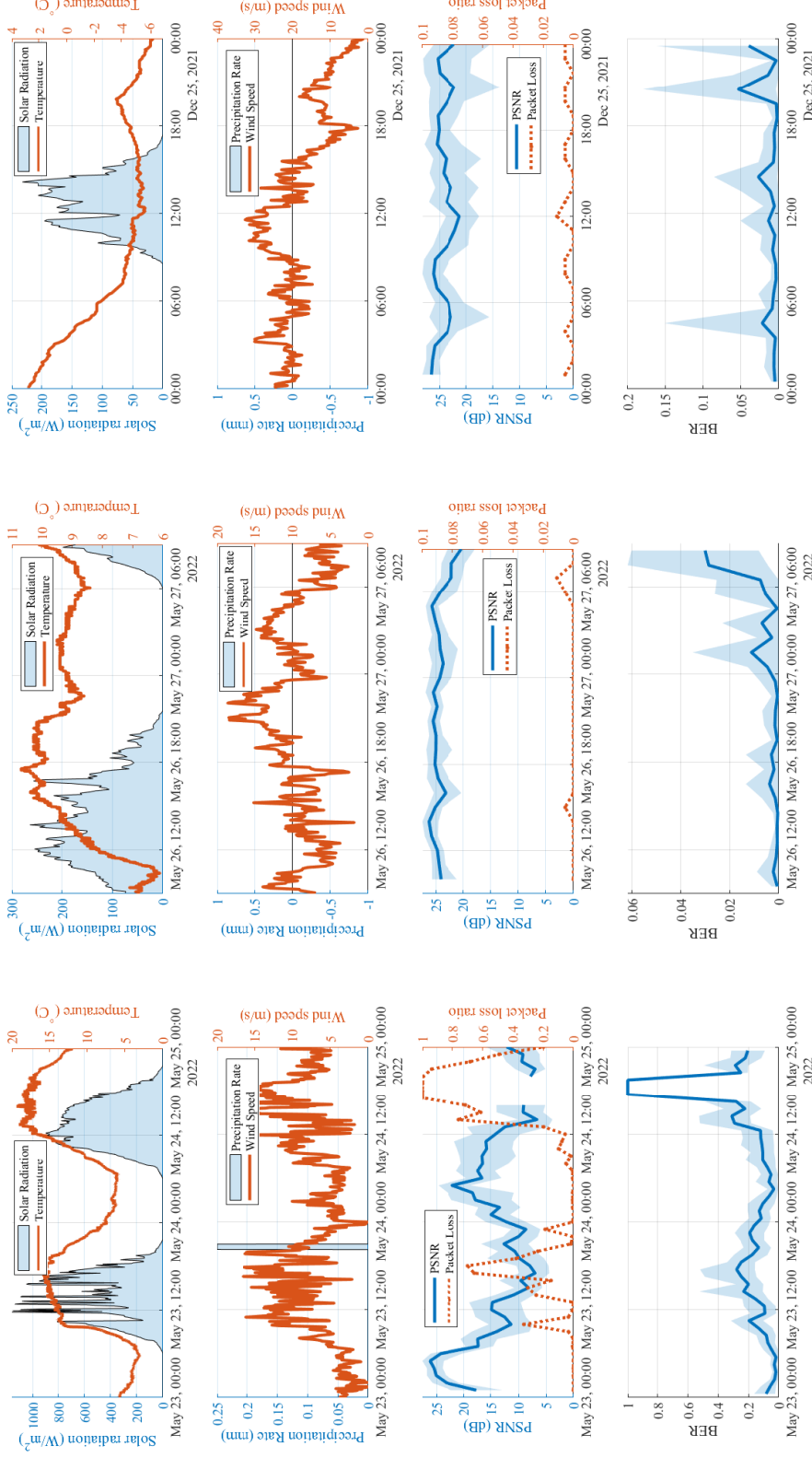


Figure 3.7: Case Study 3.1 weather information and communication performances (Row 1: Air temperature and solar radiation; Row 2: Wind speed and precipitation rate; Row 3: Packet loss ratio and packet header PSNR; Row 4: data block BER. Left column: Summer sunny days; middle column: Summer cloudy days; Right column: Winter open water)

The results from the two sunny summer days are shown in the left column of Figure 3.7. It is shown that both the packet loss ratio and BER increase and the PSNR decreases when the solar radiation and temperature decrease due to the sunset. For data during a gloomy summer day shown in the middle column and a winter day in the right column, the variation ranges of temperature and solar radiation rate are smaller, which leads to better UWA communication performances with higher PSNR and lower packet loss ratio and BER. This can be a good training data set case for reinforcement learning studies that try to schedule UWA communication at optimal time windows.

We measured the SSP at Node A once every hour during a summer day. The sound speed range at different times with corresponding temperature and solar radiation rate is shown in Figure 3.8 to Figure 3.10. The water temperature distribution is a cumulative effect of the air temperature and solar radiation, as well as the SSP. It shows that the sound speed range is more extensive during dusk, similar to the time ranges when the UWA channel becomes challenging in Figure 3.7.

We simulated ray tracing of the acoustic wave with the BELLHOP simulator to validate our assumption that the inhomogeneous water temperature distribution leads to different UWA channel conditions in the river. In Figure 3.11 to 3.13, the ray tracing is simulated with the SSP measured near Node A at three different times, namely at the summer dusk, at summer night, and in winter. The water depth

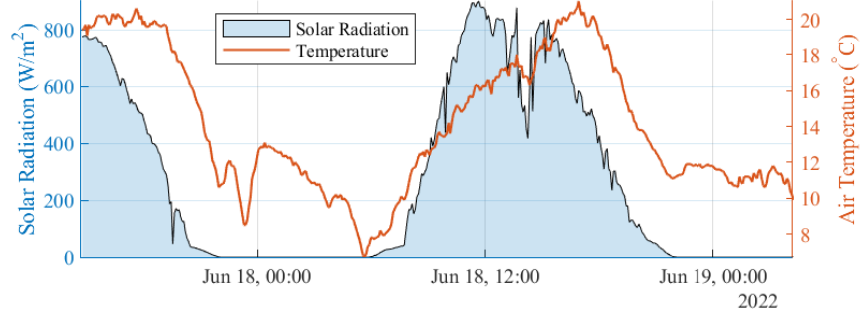


Figure 3.8: Air temperature and solar radiation

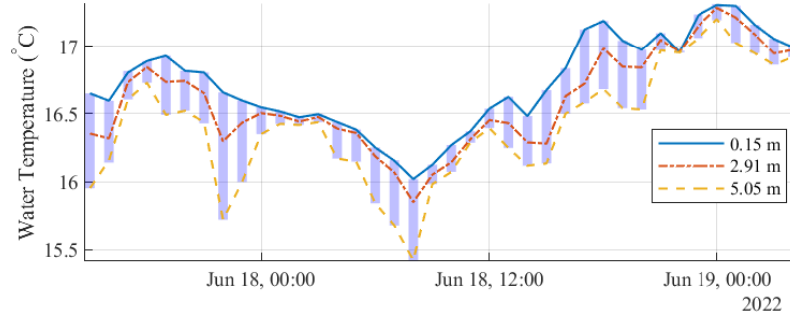


Figure 3.9: Hourly water temperature range

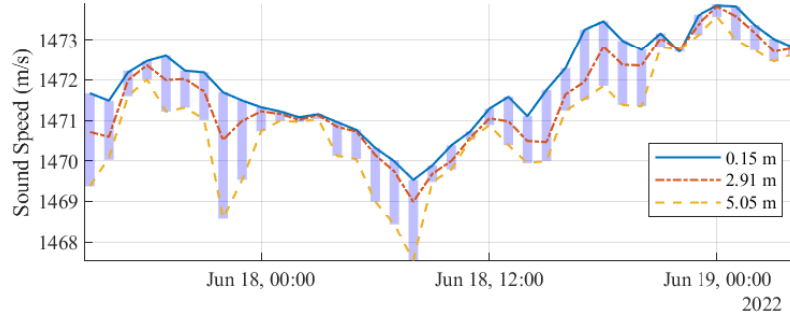


Figure 3.10: Hourly sound speed range

in these simulations is similar to the natural environment's UWA channel between Node A and Node B. Green lines denote rays with surface reflections only, blue lines denote rays with bottom reflections only, red lines denote rays with neither surface nor bottom reflection, and black lines denote rays with both surface and bottom reflections. The solid black lines are rays with no more than 4 reflections, and the

dot-dashed black lines are rays with 4 to 6 reflections in total.

With the given water depth and communication distance, the observed temperature differences at summer dusk and winter are significant enough to eliminate the line-of-sight ray between the transmitter and the receiver. When the surface water temperature is higher on sunny summer days, the sound speed is higher at the shallower depth, which leads to the sound rays bending towards the bottom, as shown in Fig. 3.11. When the surface water temperature is lower in winter, the sound speed is higher at the deeper depth, which leads to the sound rays bending towards the surface, as shown in Fig. 3.13. With the surface and bottom reflection losses set to empirical values of 1 and 10, respectively [47], the simulated CIRs of these three cases are shown in Fig. 3.14. The summer dusk case suffers the most severe attenuation, while the delay spread for the winter case lasts the longest time.

3.5 Case Study 3.2: Water Surface Condition

The water surface condition can be affected by wind speed and precipitation rate. As shown in Figure 3.15 and Figure 3.17, when the precipitation rate increases, the PSNR decreases while the packet loss ratio and BER increase. Also, the 90% middle-value range of these UWA communication performance-related parameters is wider when the precipitation rate and wind speed are higher.

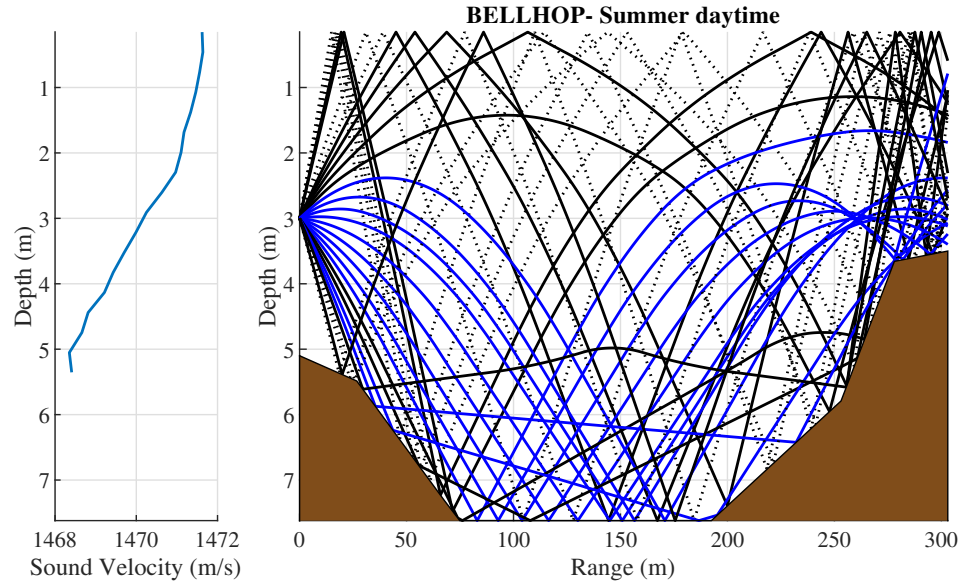


Figure 3.11: BELLHOP simulation with SSP measured at 2022-06-17 21:59

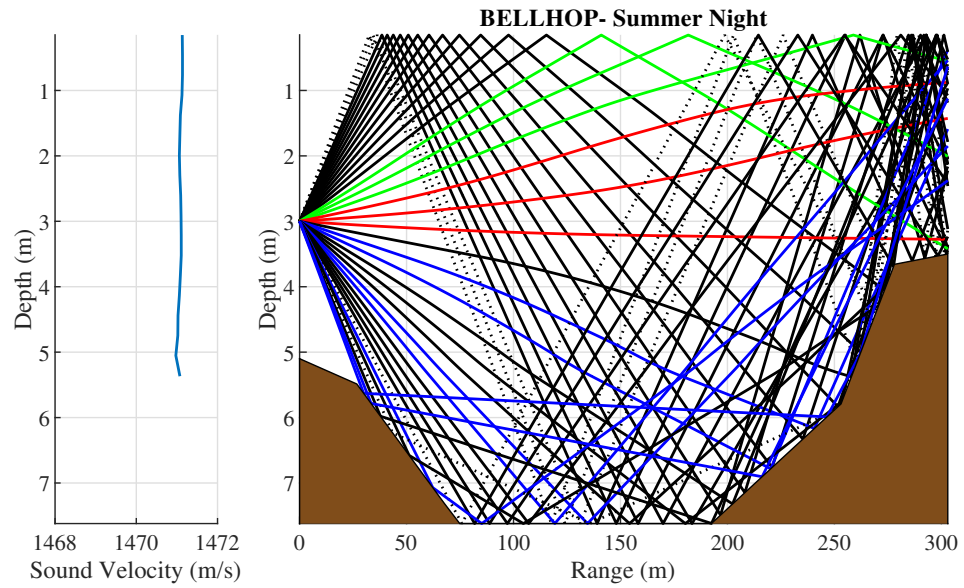


Figure 3.12: BELLHOP simulation with SSP measured at 2022-06-18 01:00

During the experiment shown in the right column of Figure 3.7, the water surface was covered with thin ice and snow. Comparing to the right column of Figure 3.15, the

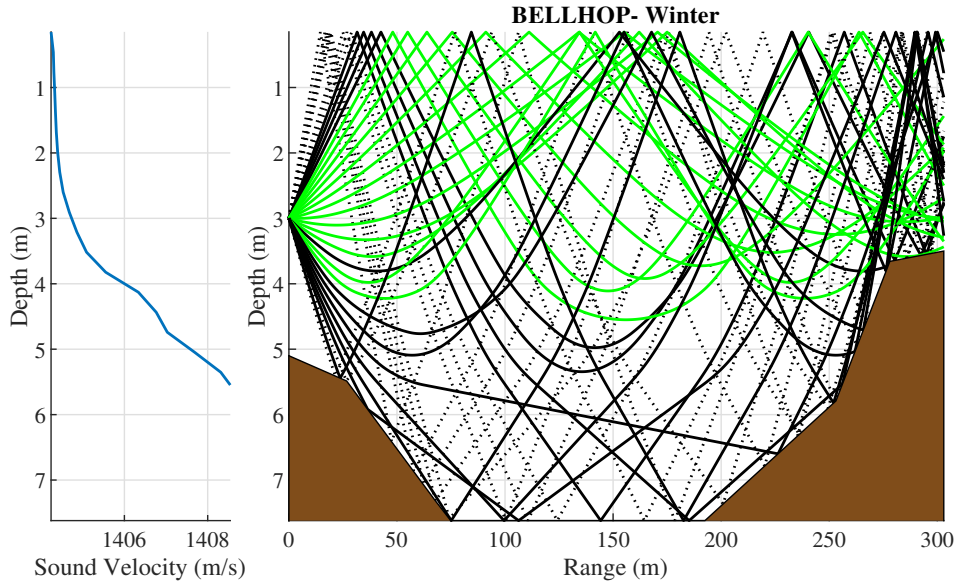


Figure 3.13: BELLHOP simulation with SSP measured at 2020-03-06 17:40

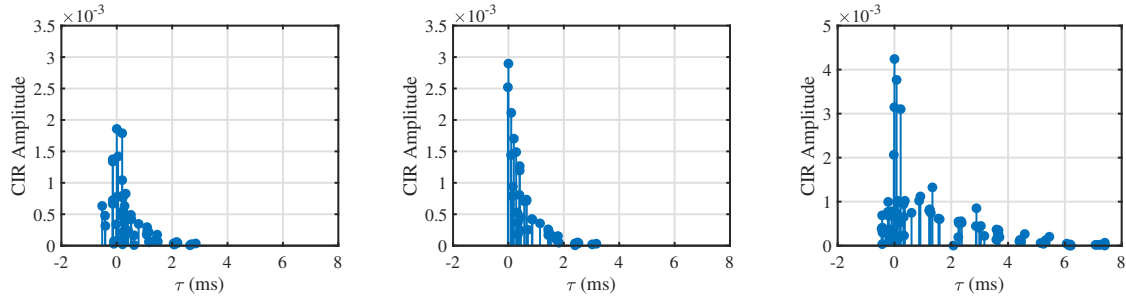


Figure 3.14: BELLHOP simulated channel impulse response delay profiles.
(left: summer dusk, middle: summer night, right: winter)

average PSNRs are at a similar level for open water and ice-covered cases, but the 90% middle-value range of the ice-covered case is larger even when the wind speed is lower.

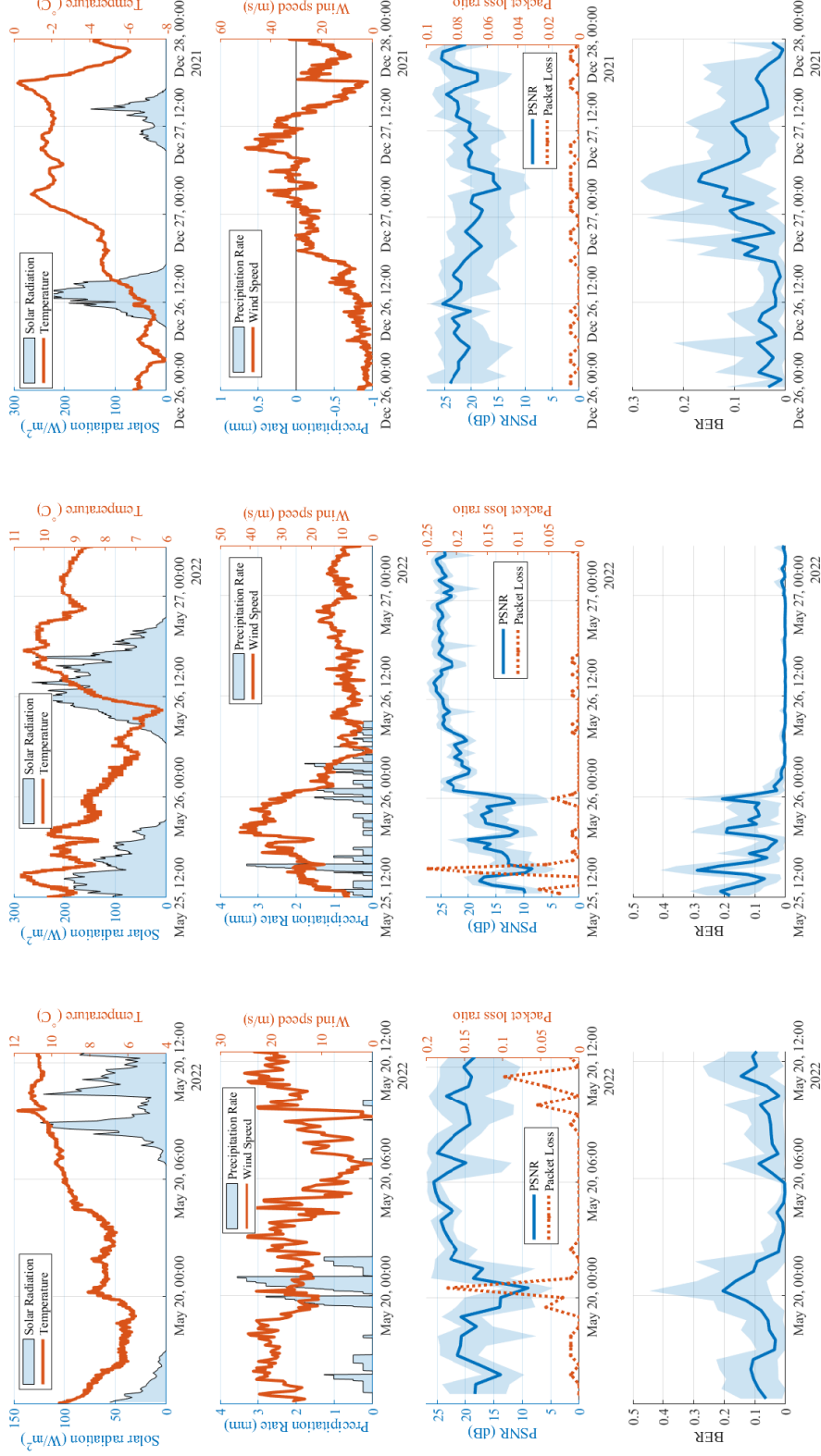


Figure 3.15: Case Study 3.2 weather information and communication performances (Row 1: Air temperature and solar radiation; Row 2: Wind speed and precipitation rate; Row 3: Packet loss ratio and packet header PSNR; Row 4: data block BER. Left column: Rainy and cloudy days 1; middle column: Rainy and cloudy days 2; Right column: Winter windy days)

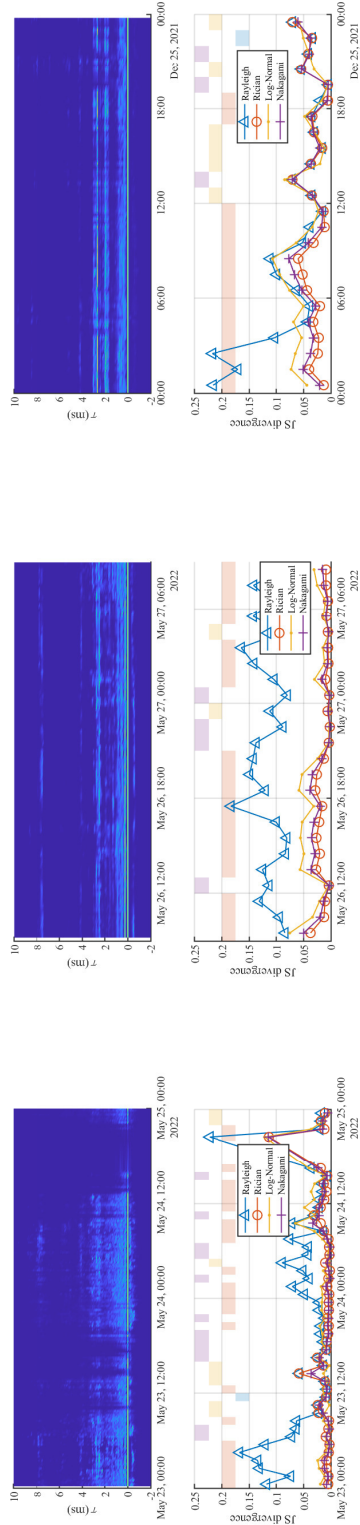


Figure 3.16: Case Study 3.1 Histogram of delay of significant peaks at Node C and main tap gain distribution

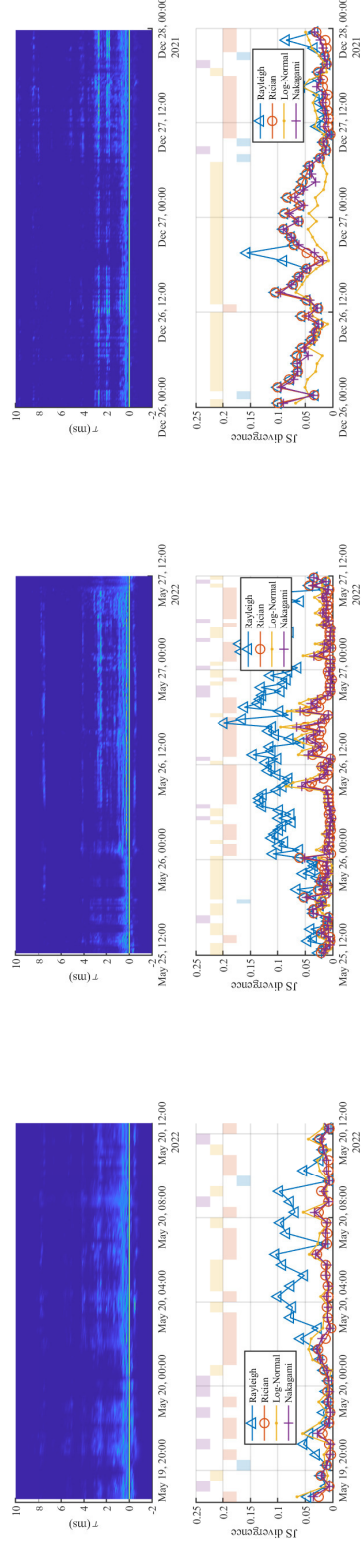


Figure 3.17: Case Study 3.2 Histogram of delay of significant peaks at Node C and main tap gain distribution

3.6 Case Study 3.3: Flood

Although there was a weather station measuring the weather conditions at the sender node, there were other environmental factors significantly affecting the UWA channel. As shown in Figure 3.18, there was neither a high solar radiation rate during day time nor severe air temperature changes. Figure 3.19 shows that there was heavy rain with a strong wind at midnight on April 23, 2022. However, as shown in Figure 3.20 and 3.21, during the following day, the UWA channel conditions remained in a bad state with no strong solar radiation nor wind and rain. The flood alert announced by the local government may explain why the UWA channel in the river was not similar to the cloudy day cases shown in Case Study 3.1 and 3.2.

3.7 Case Study 3.4: Ice Eater

There was equipment named ice eater near Node B. It periodically pumps the bottom water to the surface to keep the dock from freezing. As shown in Figure 3.22 to 3.25, the UWA channel conditions were significantly affected by the operating ice eater. As clearly shown in Figure 3.24, the significant peaks suddenly converged when the ice eater was turned on. The PSNR and BER also periodically varied with the ice eater operating time but with some delayed effects.

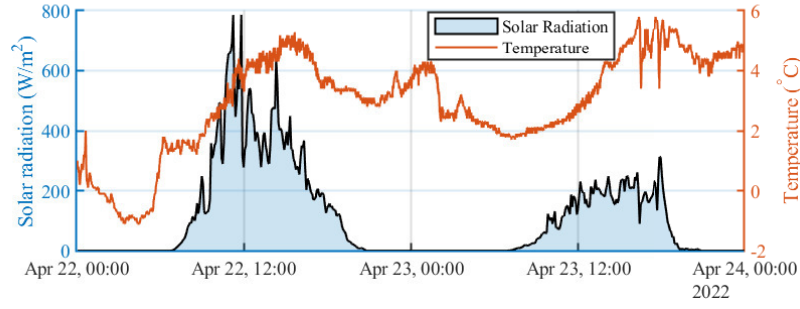


Figure 3.18: Air temperature and solar radiation

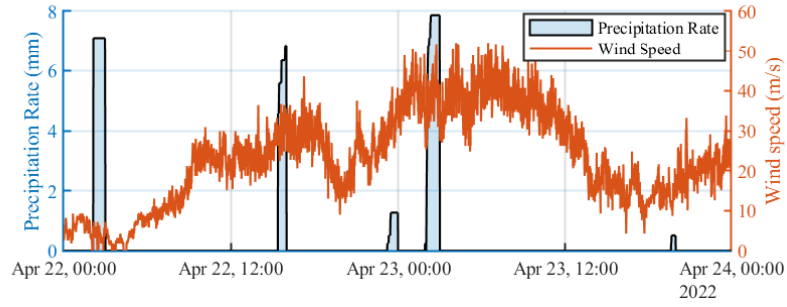


Figure 3.19: Wind speed and precipitation rate

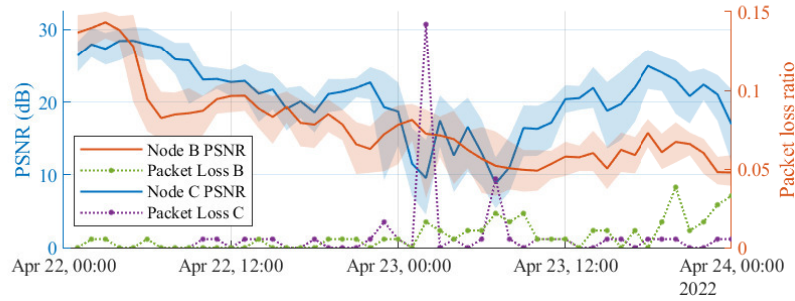


Figure 3.20: Packet loss ratio and PSNR of packet header

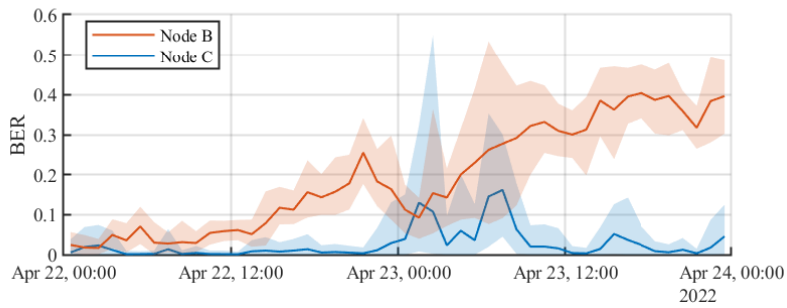


Figure 3.21: BER during flooding

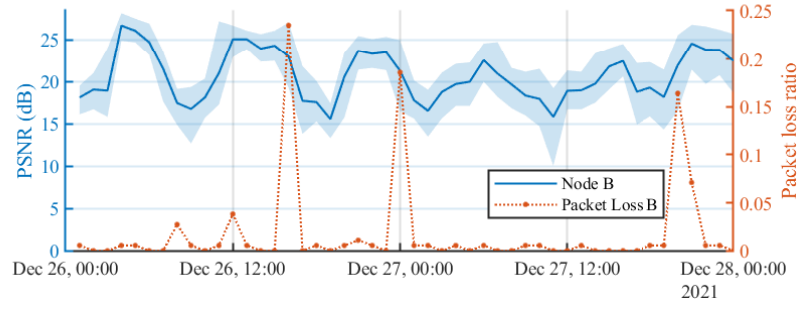


Figure 3.22: PSNR and packet loss ratio at Node B

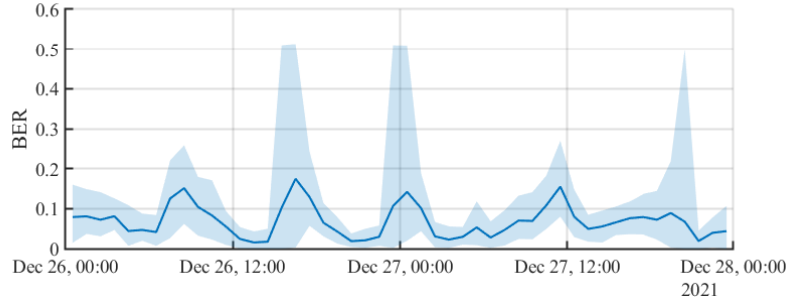


Figure 3.23: BER at Node B

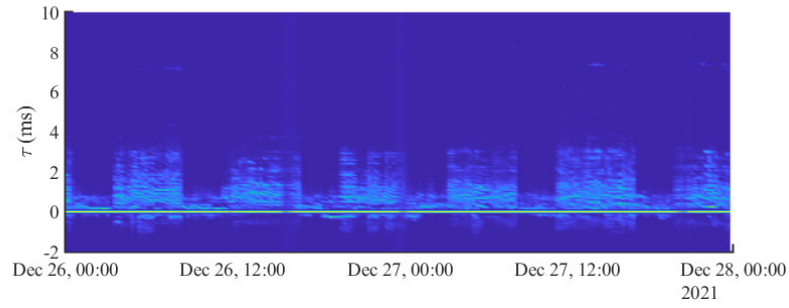


Figure 3.24: Delay distribution of significant peaks

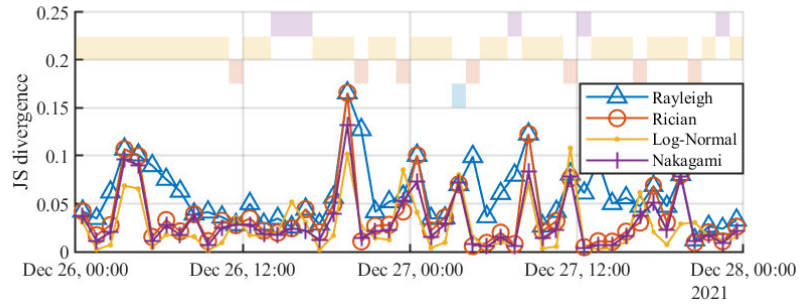


Figure 3.25: Histogram fit of the strongest peak

3.8 Summary of the experiment

The proposed system has been deployed at three different seasons in a year for a series of UWA channel experiments. An OFDM waveform has been intensely transmitted three times per minute for several days during each deployment under different weather conditions. An ensemble of millions of OFDM waveform has been collected with corresponding weather information, which could benefit the adapting of deep learning models to the UWA communication research.

The temperature profile strongly affects the UWA communication performance since it determines the refraction patterns of the acoustic waveform in the water. The observed daily solar radiation and temperature changes can significantly affect the temperature profile and UWA channel.

The precipitation rate affects both the surface condition and the temperature profile, which leads to the UWA communication performance decreasing and varying in a more extensive range.

Chapter 4

A Deep Generative Model for Underwater Acoustic Channel Impulse Response

The stochastic CIR models have elusive mathematical descriptions which need intractable assumptions with detailed environmental data. The parameters of such models are difficult to estimate from the experiment observations due to the poorly understanding of detailed underlying physics. The Deep generative models [48] can learn from a target data distribution and generates new samples following a similar distribution, but no prior knowledge about the stochastic distribution types is needed.

The objective of modeling the UWA CIR with a deep generative model is to learn a representation of the observed CIR distribution with a neural network. The CIR samples following a similar distribution to the experiment observation can be generated by the deep generative model with samples drawn from standard random distributions. These generated CIR samples can be used for predicting the performances of communication configuration options by the cognitive UWA communication system.

This chapter presents a conditional generative adversarial network model for modeling the observed UWA CIR in the field experiments introduced in Chapter 3. A Wasserstein loss is employed to relieve the mode collapse issue of the generator. To evaluate the similarity of the generated CIR distribution to the experiment observations, the power weighted JSD is proposed to measure the overall performance of the generative models for UWA CIR.

Part of this chapter was published at the 15th International Conference on Underwater Networks Systems (WUWNet21), November 22-24, 2021, Shenzhen, Guangdong, China [49] (<https://doi.org/10.1145/3491315.3491330>).

4.1 Related Work

The UWA channel characteristics have been studied with both modeling and experimentation methodologies for decades [50]. UWA channels have been represented as mathematical models or simulation models. The mathematical models describe the variations of an acoustic waveform when propagating through a UWA channel, which play an important role in the design and analysis of UWA communication systems. However, tractable mathematical descriptions of a UWA communication channel are elusive due to the complexity that how environmental parameters affect sound propagation, reflection, refraction, scattering, and reverberation. The simulation models can generate UWA channel realizations based on mathematical models describing the variation of acoustic waveforms [50], stochastic models describing the distributions of UWA channel randomness [41], and/or replays of the measured channel condition in experiments [51]. Most existing simulation systems can simulate certain aspects of the UWA channel, but few systems have demonstrated the capability of simulating the UWA channel which can match the data over a time scale that is appropriate for UWA communications [13].

On the other hand, performance evaluation of practical UWA communication systems still relies heavily on extensive field experiments due to the lack of well-categorized

channel types and corresponding stochastic models. Although several field experiment test-beds have been developed in past years, the field experiments are still costly and have limited opportunity for repeating tests [28]. The re-usability of field experiment data is limited since field experiments are usually tailored to a particular communication scheme. Even for the same communication scheme, data obtained at different experiment sites could be distinctive due to the geographic and hydro-graphic differences of UWA channels. Thus, a UWA channel model with high validity and re-usability is widely demanded due to the limitations of existing mathematical models, simulation models, and field experiments.

Deep learning has been found in a wide range of applications in wireless communication systems in recent years. Several researchers have explored utilizing auto-encoder based models for solving various wireless communication problems. The encoder and decoder perform signal processing at the transmitter and the receiver, respectively. Traditional digital signal processing modules, such as error correction coding, components of the modulation and demodulation, and detection, are implemented as the encoder at the transmitter and as the decoder at the receiver. The auto-encoder is trained as parts of a communication system including a transmitter, a receiver, and a channel model in between. Other signal processing modules at the transmitter and receiver side are also included in the overall input-output of the auto-encoder, as well as the distortions and noises added to the signal by the channel. Existing auto-encoder based communication system design work has been reviewed in [52] and [53].

However, most existing works suffer from the curse of dimensionality and can only be evaluated with a simple additive white Gaussian noise (AWGN) channel model. Another type of the auto-encoder application for wireless communication is using an auto-encoder to compress the downlink channel state information (CSI) of multiple-input multiple-output (MIMO) wireless communication systems to reduce the CSI feedback overhead. An optional channel model can also be involved in the training process of the auto-encoder to enhance the overall robustness of the compressed MIMO CSI feedback. Related works for this application have been summarized in [54]. An auto-encoder consisting of residual network blocks was employed in [55] to reduce the dimensionality of CSI representations. Furthermore, an extended neural network structure with a learning rate scheduling scheme was proposed in [56] to enhance the MIMO CSI compression performances. Both works demonstrated practical scales and architectures of deep neural networks for representation learning of CSI data, which have significant referential value for VAE design of CSI generative models.

The RF MIMO CIR data set COST2100 [57] was used to train many deep learning models for wireless communication. In [58], a GAN model is employed to learn the distribution of the COST2100 data set. There are also VAE based models, such as CsiNet [55] and CRNet [56], learn a latent representation of the COST2100 CIR sample to reduce the CSI feedback overhead, which can also be converted to generative models by sampling in the latent space. However, since there as no observable

correlations between the COST2100 CIR samples and any temporal or environmental factors, the COST2100 data set was considered following a distribution without conditional inputs in these works.

In [49], a VAE model trained with the KWAUG14 data set was proposed as the first generative model for UWA CIRs. Due to the lack of training data set, the UWA CIRs were also considered following a distribution without conditional inputs. The generated UWA CIR samples can reflect some of the characteristics of the experiment data. However, there was no performance metrics for measuring the similarity of the generated distribution to the experiment data.

4.2 Wasserstein Conditional Generative Adversarial Network for UWA CIR

A conditional generative adversarial network (CGAN) [59] consists of a generator and a discriminator. The inputs of the generator include the conditional variable and the random vector drawn from a prior standard distribution. The generator can convert the input to a data sample that is similar to the target data set samples. The inputs of the discriminator of the CGAN also consist of two components, namely the conditional variable and the generated or target data sample. The discriminator outputs the likelihood of the input data sample combined with the conditional variable

is from the target data set.

The CGAN for the UWA CIR data set is shown in Figure 4.1. The values of the 100x1 random vector z are drawn from a standard Normal distribution. The conditional variable vector θ consists of six values, including the timestamp of the CIR sample and its real-time weather information. The timestamp consists of the date of a year and the time of a day, which are normalized between 0 to 1. The real-time weather information is the normalized latest weather station reading including the air temperature, the solar radiation rate, the wind speed, and the precipitation rate.

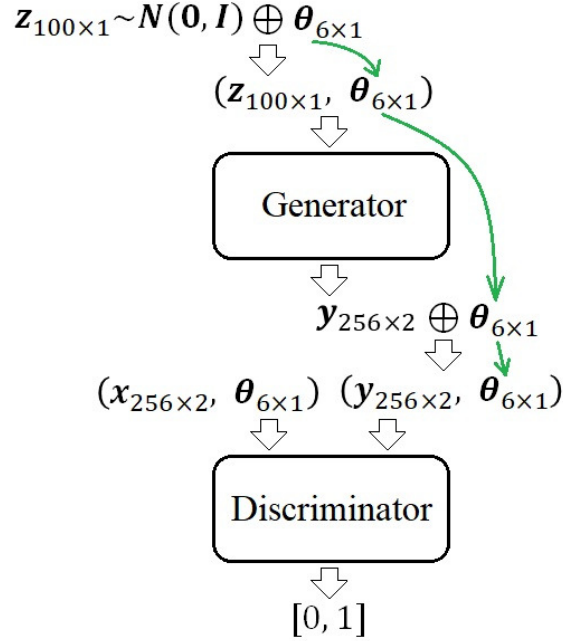


Figure 4.1: Conditional generative model for UWA CIR

The generator and discriminator are multilayer perceptrons (MLP) consisting of 4 fully connected linear layers, as shown in Table 4.1 and 4.2. The first 3 linear layers of the generator are followed by a leaky ReLU activation function ($\alpha = 0.2$). The

activation function of the last linear layer for the generator is the *tanh* function. The first 3 linear layers of the discriminator are followed by a leaky ReLU activation function ($\alpha = 0.3$) and a dropout layer ($p = 0.3$). The last linear layer of the discriminator is followed by a *Sigmoid* activation function.

Table 4.1
Summary of the WCGAN generator network

Layer type	Input dim	Output dim	Parameters
Linear	100 + 6	256	27392
LeakyReLU ($\alpha = 0.2$)			
Linear	256	512	131584
LeakyReLU ($\alpha = 0.2$)			
Linear	512	1024	525312
LeakyReLU ($\alpha = 0.2$)			
Linear	1024	512	524800
Tanh			
Total			1209088

Table 4.2
Summary of the WCGAN discriminator network

Layer type	Input dim	Output dim	Parameters
Linear	256x2 + 6	1024	531456
LeakyReLU ($\alpha = 0.3$)			
Dropout ($p = 0.3$)			
Linear	1024	512	524800
LeakyReLU ($\alpha = 0.3$)			
Dropout ($p = 0.3$)			
Linear	512	256	131328
LeakyReLU ($\alpha = 0.3$)			
Dropout ($p = 0.3$)			
Linear	256	1	257
Sigmoid			
Total			1187841

4.3 Training the WCGAN

The objective of the Wasserstein GAN [60] as shown in Equation 4.1 is employed for training the proposed WCGAN. A gradient penalty term in [61] is employed for training the discriminator.

$$\min_G \max_D \mathbb{E}_{\mathbf{x} \sim \mathbb{P}_x} [D(\mathbf{x}, \theta)] - \mathbb{E}_{\mathbf{z} \sim \mathbf{N}(\mathbf{0}, \mathbf{I})} [D(G(\mathbf{z}, \theta), \theta)] \quad (4.1)$$

$$L_G = \mathbb{E} [-D(G(\mathbf{z}, \theta), \theta)] \quad (4.2)$$

$$L_D = \mathbb{E} [D(G(\mathbf{z}, \theta), \theta)] - \mathbb{E} [D(\mathbf{x}, \theta)] + \lambda \mathbb{E} [(\|\nabla D(G(\mathbf{z}, \theta), \theta)\|_2 - 1)^2] \quad (4.3)$$

The UWA CIR data are paired with its conditional variable θ vector and grouped to data batches of 64 samples. For each data batch, the discriminator will first be trained for 5 times with the loss function shown in Equation 4.3. The gradient penalty coefficient λ is set to 10. Then, the θ vectors of this training data batch will be shuffled and grouped with z vectors drawn from the standard Normal distribution as the inputs of the generator. The generator weights will be trained for 1 time with the loss function shown in Equation 4.2. The Adam optimizer [62] is employed to train the weights, and the learning rate is set to 0.0001. The batch losses during a training process is shown in Figure 4.2

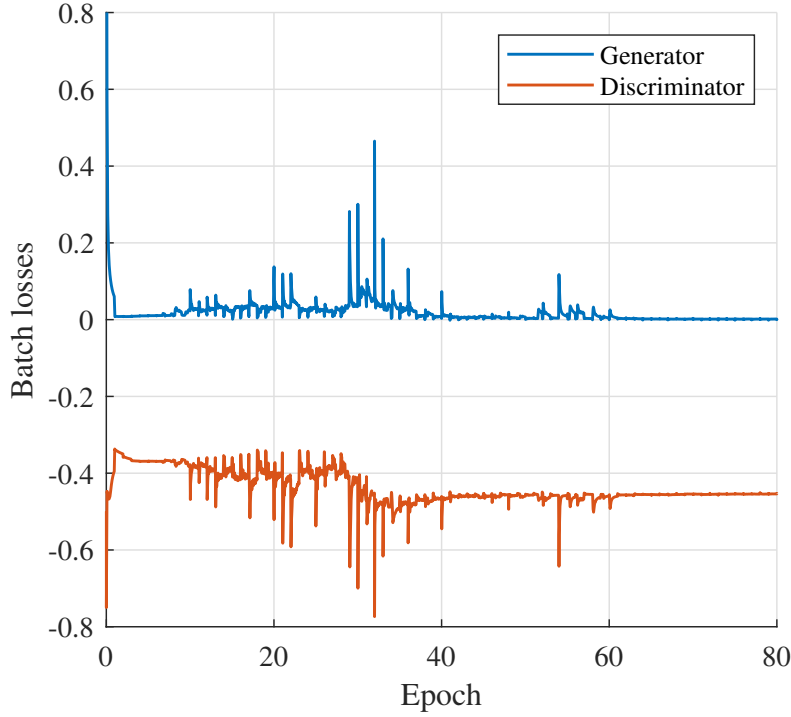


Figure 4.2: Batch losses during training

Figure 4.3 shows some examples of generated UWA CIR samples during the training process. There are five different θ values are selected to demonstrate the generated CIR samples. The odd columns are time domain amplitude of CIR samples, while the even columns are its corresponding frequency domain amplitude. The first row of Figure 4.3 are samples from the training data set, and the bottom three rows are three generated CIR samples with the same θ value as printed on the top of each training CIR sample. The generated samples show similarities to the training samples in both time and frequency domain amplitude plots. However, variations can also be observed among the three generated samples, which indicates the WCGAN has capabilities of avoiding monotonousness of the stochastic replay of UWA CIR models.

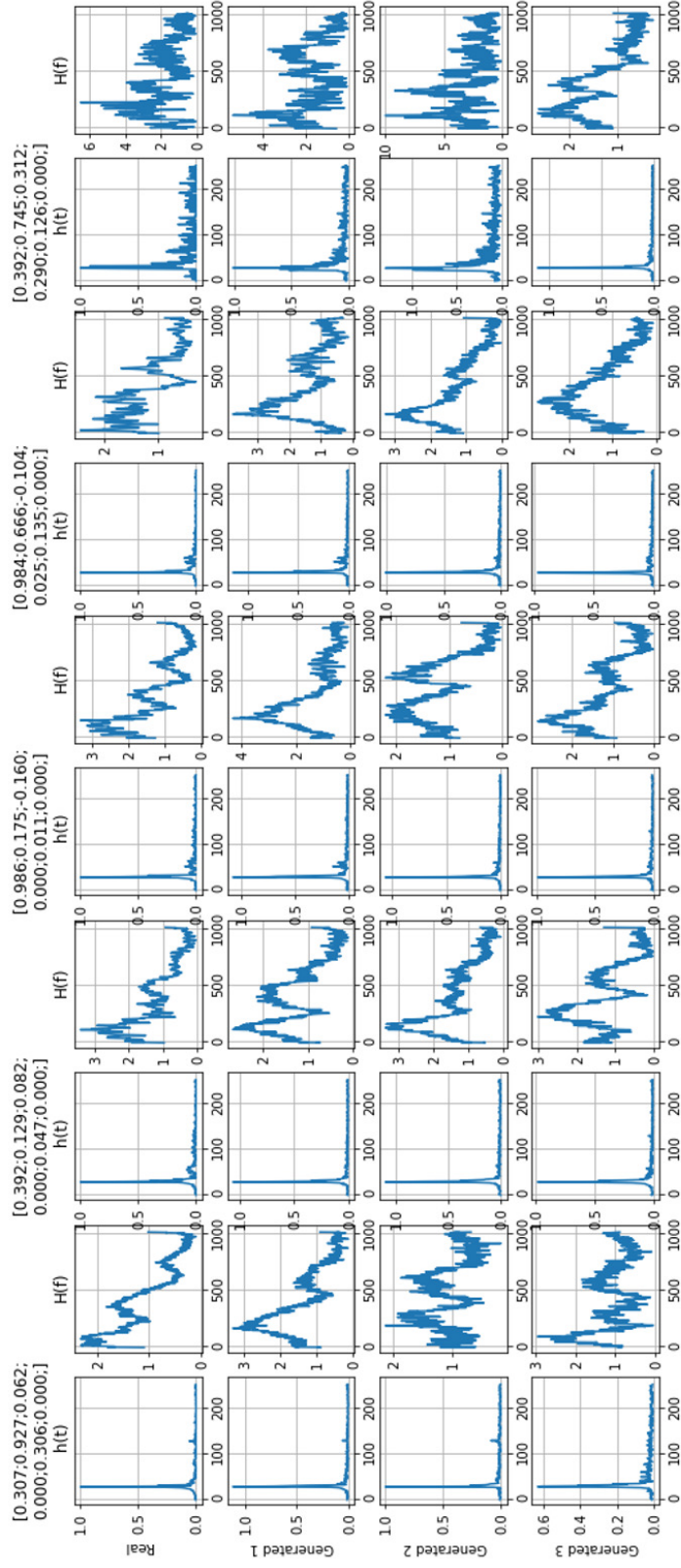


Figure 4.3: Generated samples during training

In Figure 4.4, the histograms of the 27-29th and 35-37th amplitude values of the UWA CIR samples of a 15min time window are converted to their equivalent PMFs. Besides the 29th value, the other histograms cannot be fitted to Rician, Log Normal, or Nakagami distributions by their parameter estimation algorithms. The pink lines with dot markers are the PMFs of generated CIR samples, which showed much better fitting accuracy than any of the other parametric distribution fitting results.

Especially for the fitting results of the 29th value, the observed experiment data histogram is a combination of multiple hill-shaped trends. Only the generated PMF fitted this waving trend.

For the other single spike-shaped PMFs, the Rayleigh distribution cannot fit well due to a large amount of values close to zero. This could be a result of the amplitude of a specific path diluted to multiple pixels of the CIR vector due to the varying arrival time of the path.

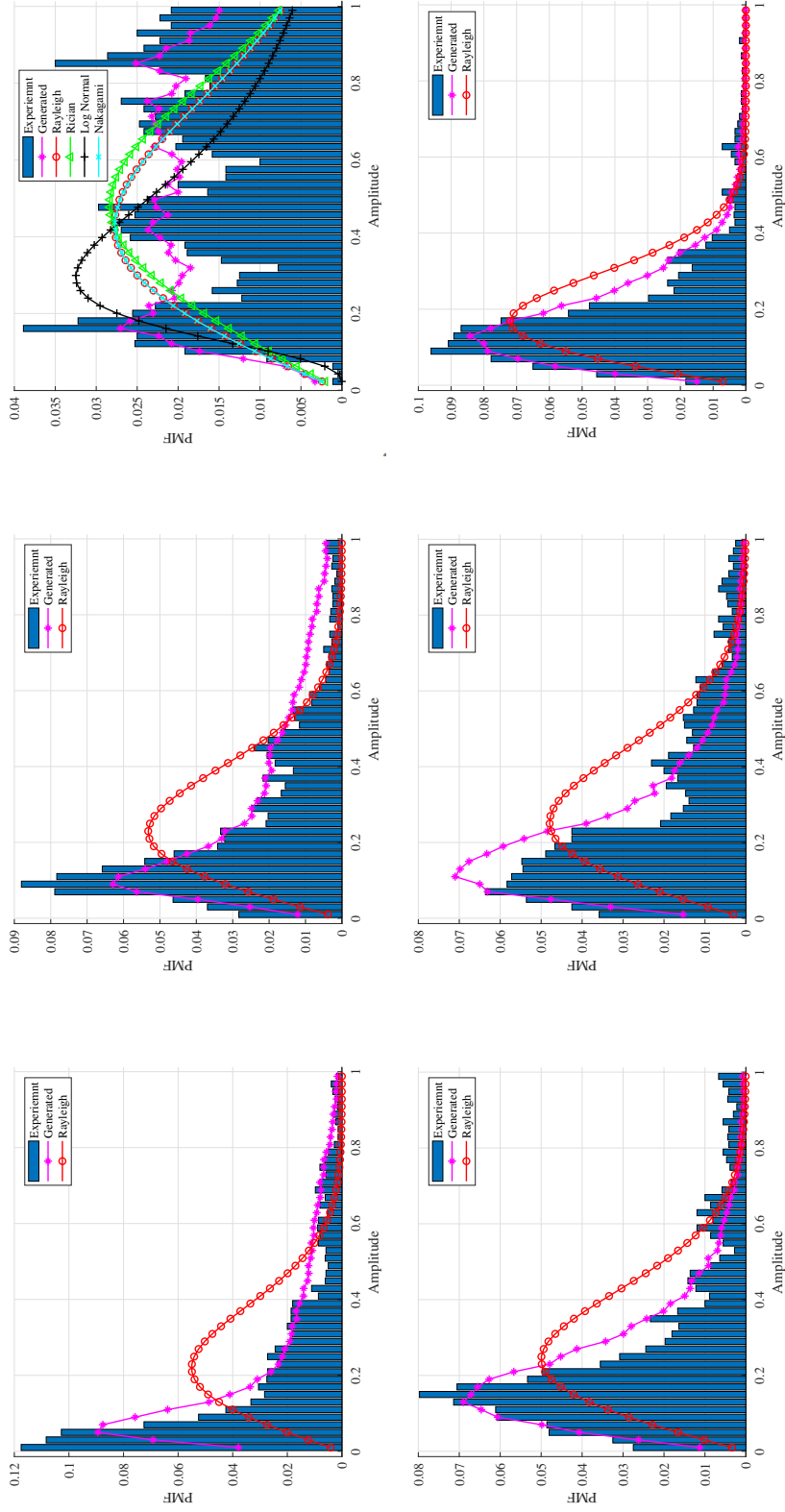


Figure 4.4: Amplitude histogram comparison examples (Row 1: Pixel 27, 28, 29; Row 2: Pixel 35, 36, 37)

4.4 Power weighted JSD

Since there are 256 values for a CIR sample, we can obtain 256 JSDs for histogram the generated CIR samples within a time window. To compare the overall similarity of the generated CIR distribution to the experiment observations, here we first calculate the mean amplitude of the experiment observations at the 256 pixels as shown in the right figure of Figure 4.5. Then, the JSD values at each pixel can be weighted by the mean amplitude, and the power weighted JSD can be obtained by

$$\text{Power Weighted JSD} = \sum_{i=1}^{256} \text{JSD}(|y_i|, |x_i|) \cdot |\bar{x}_i| \quad (4.4)$$

where x_i, y_i is the i th value of the experimental observed and generated CIR samples, respectively.

The training data set consists of 858 15-minute time windows. The mean power weighted JSD for the WCGAN generated samples of all time windows is 0.2679, while for Rayleigh distribution fitting is 0.5228. A comparison of the histograms of power weighted JSDs of 858 time windows for Rayleigh distribution fitting, WCGAN, and CGAN is shown in 4.6. The mode collapse prevention design is necessary since the vanilla CGAN performance is even worse than the Rayleigh distribution fitting.

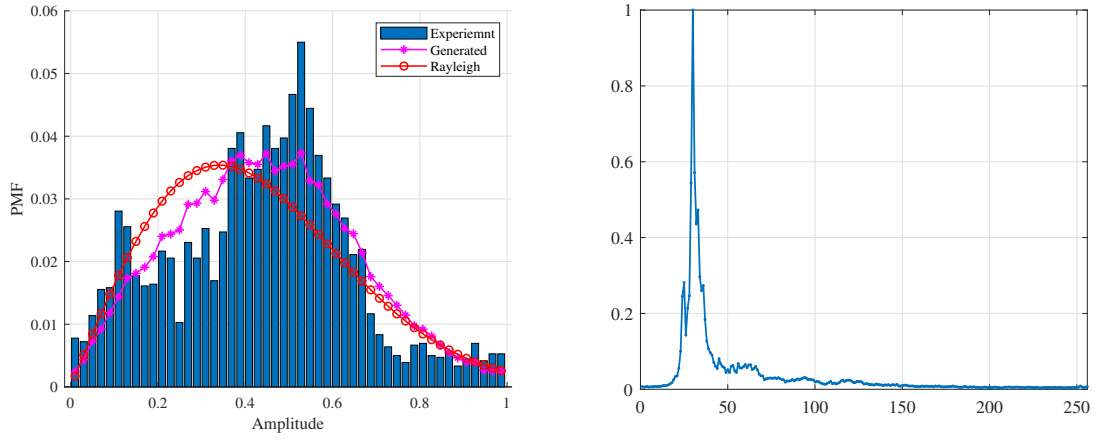


Figure 4.5: Power-weighted JSDs calculation (Left: amplitude histogram example of Pixel 32; Right: mean amplitudes of all 256 pixels for this time window)

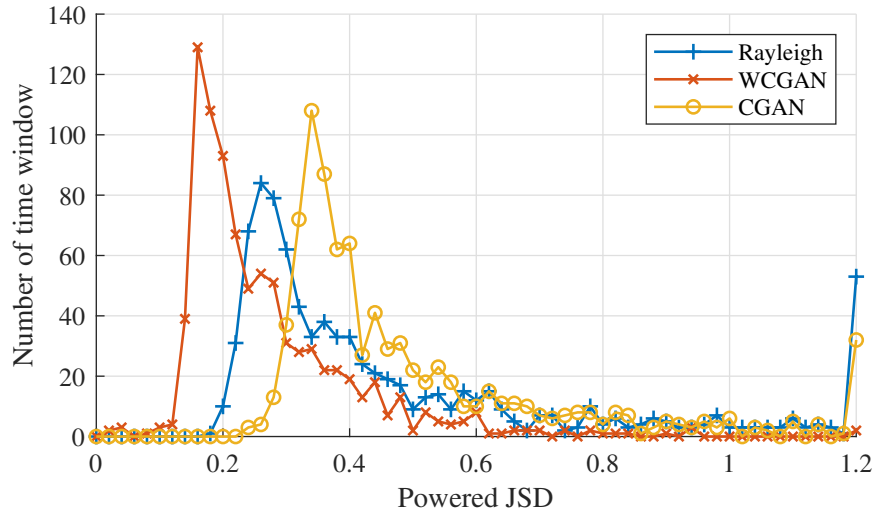


Figure 4.6: Power-weighted JSDs of the WCGAN, CGAN, and fitted Rayleigh distribution

Table 4.3

Mean power-weighted JSD of the WCGAN, CGAN, and Rayleigh fitting

WCGAN	CGAN	Rayleigh
0.2679	0.5063	0.5228

4.5 Tuning the conditional variable for generating

By tuning one of the six values in the θ vector, we can obtain generated CIR samples shown in Figure 4.7 to 4.9. It seems that each θ vector has different sensitivities on these six values. All three examples show high sensitivities on the two values corresponding to the time stamp and the temperature. However, the generated CIR based on the θ vector in Figure 4.7 is not sensitive to variations in solar radiation, wind speed, and precipitation rate. While, the generated CIR based on the θ vector in Figure 4.8 is sensitive to solar radiation and wind speed, but not to precipitation rate. The generated CIR based on the θ vector in Figure 4.9 is sensitive to all 6 values, but its variations in amplitude are not as significant as the other two examples.

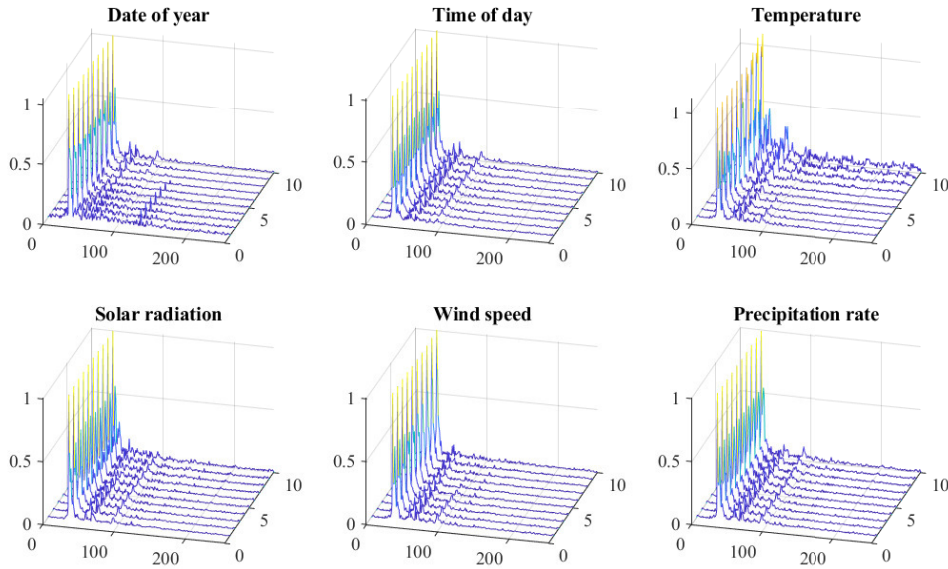


Figure 4.7: Generated CIR samples by varying each Θ value Example 1

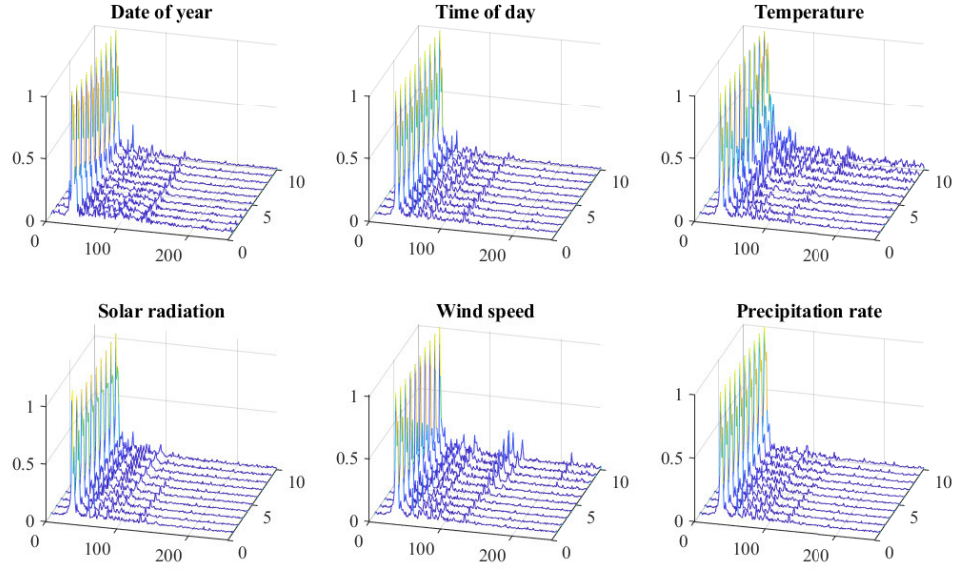


Figure 4.8: Generated CIR samples by varying each Θ value Example 2

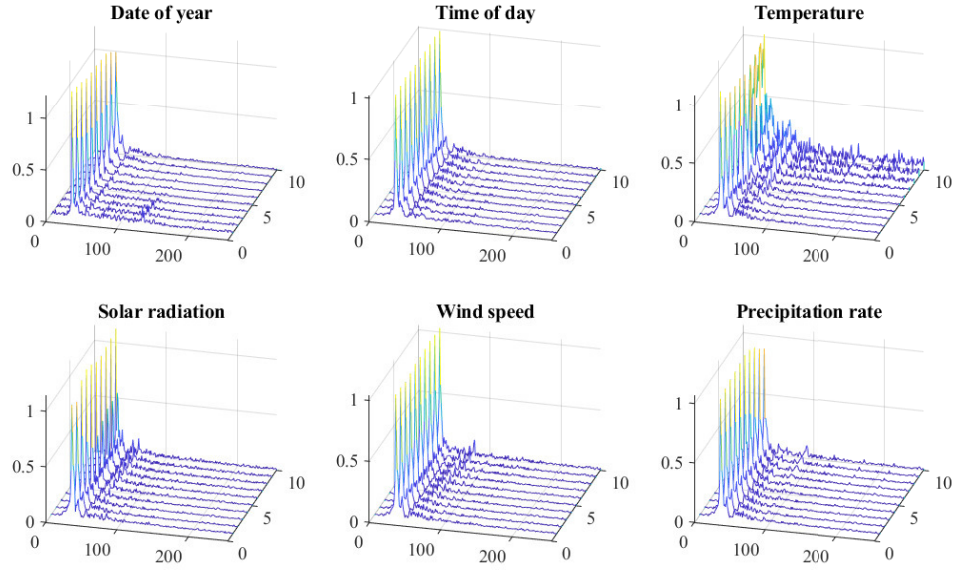


Figure 4.9: Generated CIR samples by varying each Θ value Example 3

Thus, predicting CIR distributions by interpolating conditional variables θ values is not appropriate based on current training results.

4.6 Summary of the WCGAN

A WCGAN is proposed to learn the distributions of field experiment UWA CIR samples. A power-weighted JSD measurement is proposed to evaluate the overall similarity of a generated CIR distribution to the field experiment data distribution. The WCGAN outperforms the conventional stochastic distribution fitting methods from the mean power-weighted JSD perspective.

The performance comparison between the WCGAN and a vanilla CGAN showed that the mode collapse prevention designs, such as the Wasserstein loss, are essential for modeling UWA CIR distributions with deep generative models.

Chapter 5

Prediction of the CIR distribution

As results shown in Section 4.5, predictions of CIR distribution cannot be accomplished by simply interpolating conditional inputs of WCGAN.

From the observations discussed in Section 3.4, on summer sunny days, the water temperature distribution can be significantly affected by the solar radiation rate and air temperature. As a cumulative result of the solar radiation and air temperature, the large temperature differences at different depths will lead to a harsh UWA communication channel condition. For energy efficiency concerns, a smart UWA communication system should be able to learn to avoid UWA transmissions under such predictable channel conditions. The prediction of these harsh channel conditions should be achievable by deep learning models based on historical weather conditions.

The objective of CIR distribution prediction is ultimately for predicting the performances of different communication configuration options for a UWA cognitive communication system. In a communication scenario, the sender and the receiver can have a few rounds of brief information exchange at the beginning stage of a data transfer task, such as the handshaking to establish a link or several trials of data transfer at the beginning. Hence, a few CIR samples can be obtained before the communication configuration is determined for the following data transfer activities. Thus, the prediction of the CIR distribution can be focused only predict the near-future channel states based on a recent CIR observation and the future weather information forecast from others.

This chapter presents a CGAN based prediction model for UWA CIR. The prediction results are also evaluated from the power-weighted JSD perspective.

5.1 Related Work

The study of UWA channel characteristics plays an important role in the design, analysis, and performance evaluation processes of these novel UWA communication schemes. Therefore, a UWA channel model with high validity and re-usability is widely demanded. Such an effective model is expected to have several layers of complexity that can reflect the deterministic characteristics of acoustic propagation in a

certain geographical environment, as well as the stochastic characteristics caused by large-scale and small-scale uncertainties [4].

From a communication perspective, all the spatial-temporal variations of UWA channels can be distinguished as two types based on their duration, namely large-scale and small-scale variations [41]. The large-scale variations, which span multiple communication transactions, were considered caused by uncertainties that affect the acoustic link geometry [41]. The large-scale variations were modeled as random variables that lead to variations in the gains and delays of propagation paths, which influence the SNR through its local average over a period of time [41]. On the other hand, the small-scale variations, which occur over a single communication transaction, are considered a consequence of scattering and instantaneous motion [41]. The small-scale variations were modeled as random variables that affect the instantaneous UWA channel response conditioned on a particular large-scale realization [41]. Studying the small-scale variations is meaningful for the analysis of signal processing algorithms and network protocol designs, while studying the large-scale variations can benefit the analysis of strategic system configurations, such as the transmitting power level configuration, as well as the assessment of outage probabilities and statistical coverage for using a particular modulation mode and network protocol configuration.

The prediction of CIR by deep learning has been studied from various perspectives [63]. In [64], the CsiNet proposed in [55] was employed to learn a latent representation

of the CIR to reduce the CSI feedback overhead. Then, a LSTM model was used to learn each single CIR sample as a short time sequence. By integrating the LSTM model proposed in [64] with the CsiNet, the recovery accuracy of the CSI coded in the latent space was enhanced. With the narrow band assumption of the RF channel, a CIR can be considered as a single complex value in the frequency domain. The temporal variation process of the CIR was considered as time sequence and modeled with deep learning models for sequence data. For example, a recurrent neural network (RNN) model is proposed for predicting real-world non-stationary channels in [65]. The long short term memory (LSTM) neural network is employed to model and predict the CIR in [66, 67, 68]. A LSTM based model was proposed in [69] for learning the CIRs as a time sequence. In [70], the CIR of a wide band channel was modeled as a vector of complex values, and a convolutional LSTM was employed to learn the joint spatial-spectral-temporal dependencies observed in spectrum usage. A shared characteristic of this type of works is that deep learning models are employed to predict samples in a time sequence, not the temporal variation of a distribution. Few such models can be converted to generative models that can generate predicted CIR samples with random samples drawn from a known prior.

Due to the lack of appropriate training data set and the inhered difficulties of training a GAN, it is rather challenging to use GAN based models to generate a time sequence [71]. The Time Series GAN (TSGAN) proposed in [72] employed two WGANs for generating time series data. The first WGAN generates single samples of the target

time series from random samples drawn from known prior, and the second WGAN generates the time series using the output of the first WGAN. However, GAN based time series modeling is widely used for other applications, including data augmentation [73, 74] and anomaly detection [75, 76].

5.2 CGAN based prediction model for UWA CIR

The CGAN for the UWA CIR prediction is shown in Figure 5.1. The values of the 100x1 random vector z are drawn from a standard Normal distribution. The conditional inputs of the CGAN used for prediction consist of two parts. The first part is a recently observed CIR sample \mathbf{x}_{ob} , which consists of the real and imaginary parts of the 256 complex values of a CIR sample, namely 512 input values. The second part of the conditional input is a sequence of 25 weather information samples θ during a 2-hour time window. A weather information sample consists of 4 values, namely the normalized air temperature, the solar radiation rate, the wind speed, and precipitation rate. The time interval between two samples of the sequence is 5 minutes. Based on different prediction demands, the weather information samples can be the reading from the weather station or the predicted values from the weather forecast, or a combination of both.

The generator and discriminator are multilayer perceptrons (MLP) consisting of 4

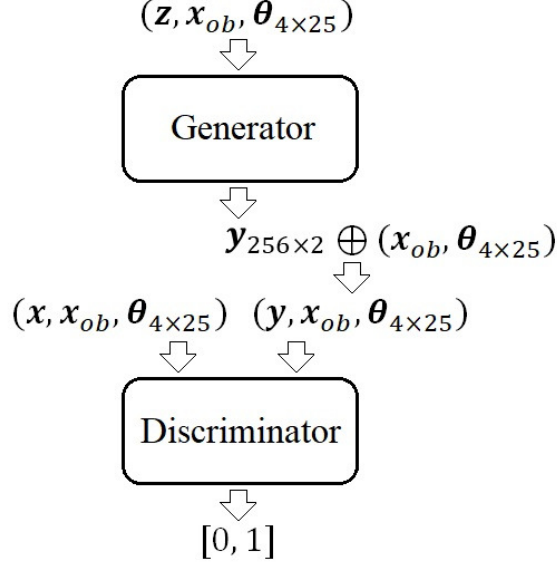


Figure 5.1: Conditional generative model for UWA CIR prediction

and 5 fully connected linear layers, respectively, as shown in Table 5.1 and 5.2. The first 3 linear layers of the generator are followed by a leaky ReLU activation function ($\alpha = 0.2$). The activation function of the last linear layer for the generator is the \tanh function. The first 4 linear layers of the discriminator are followed by a leaky ReLU activation function ($\alpha = 0.3$) and a dropout layer ($p = 0.3$). The last linear layer of the discriminator is followed by a *Sigmoid* activation function. Considering the correlations between the observed CIR \mathbf{x}_{ob} and the CIR samples to be generated, the generator can employ the residual network topology as shown in the right figure in Figure 5.2. Instead of the distribution of the training CIR samples, the MLP part of this residual network design is supposed to learn the distribution of differences between the observation \mathbf{x}_{ob} and the training CIR samples.

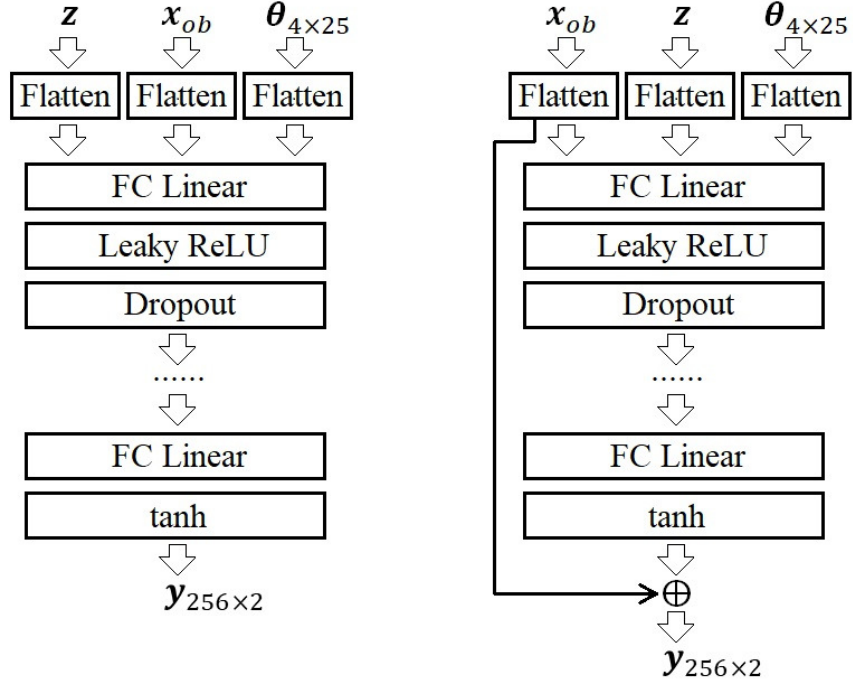


Figure 5.2: Left: original MLP fully connected generator. Right: generator with residual network structure

Table 5.1
Summary of the prediction CGAN generator network

Layer type	Input dim	Output dim	Parameters
Linear	100 + 256x2 + 25x4	1024	730112
LeakyReLU ($\alpha = 0.2$)			
Linear	1024	512	524800
LeakyReLU ($\alpha = 0.2$)			
Linear	512	1024	525312
LeakyReLU ($\alpha = 0.2$)			
Linear	1024	512	524800
Tanh			
Total			2305024

Table 5.2
Summary of the prediction CGAN discriminator network

Layer type	Input dim	Output dim	Parameters
Linear	256x2x2 + 25x4	2048	2304000
LeakyReLU ($\alpha = 0.3$)			
Dropout ($p = 0.3$)			
Linear	2048	1024	2098176
LeakyReLU ($\alpha = 0.3$)			
Dropout ($p = 0.3$)			
Linear	1024	512	524800
LeakyReLU ($\alpha = 0.3$)			
Dropout ($p = 0.3$)			
Linear	512	256	131328
LeakyReLU ($\alpha = 0.3$)			
Dropout ($p = 0.3$)			
Linear	256	1	257
Sigmoid			
Total			5058561

5.3 Training the prediction CGAN

The objective of the prediction CGAN is the vanilla CGAN loss objective as shown in Equation 5.1.

Out of the total 858 15-minute time windows, 697 time windows are selected to construct the training data set, and the rest 161 time windows are reserved as the test data set. The training data sample consists of three parts, namely the real CIR sample \mathbf{x} , an observed CIR sample \mathbf{x}_{ob} , and the sequence of weather information θ . The observed CIR sample \mathbf{x}_{ob} for each training CIR sample \mathbf{x} is selected by randomly

picking another training CIR sample within the same 15min time window. The UWA CIR data with its corresponding CIR observation \mathbf{x}_{ob} are combined with its conditional variable θ vector sequence and grouped into batches of 16 samples.

For each data batch, the discriminator will first be trained 5 times with the loss function shown in Equation 5.3, where the $H_b(*)$ is the binary cross entropy loss function as shown in Equation 5.4. Then, the paired CIR observation \mathbf{x}_{ob} and θ vector sequence of this training data batch will be shuffled and grouped with z vectors drawn from the standard Normal distribution as the inputs of the generator. The generated CIRs then will be mixed with the training data batch to train the generator weights for 1 time with the loss function shown in Equation 5.2. The Adam optimizer [62] is employed to train the weights, and the learning rate is set to 0.0001. The batch losses during a training process are shown in Figure 5.3.

$$\min_G \max_D \mathbb{E}_{\mathbf{x} \sim \mathbb{P}_x} [\log(D(\mathbf{x}, \mathbf{x}_{ob}, \theta))] - \mathbb{E}_{\mathbf{z} \sim \mathcal{N}(\mathbf{0}, \mathbf{I})} [\log(1 - D(G(\mathbf{z}, \mathbf{x}_{ob}, \theta), \mathbf{x}_{ob}, \theta))] \quad (5.1)$$

$$L_G = H_b(D(G(\mathbf{z}, \mathbf{x}_{ob}, \theta), \mathbf{x}_{ob}, \theta), 1) \quad (5.2)$$

$$L_D = H_b(D(G(\mathbf{z}, \mathbf{x}_{ob}, \theta), \mathbf{x}_{ob}, \theta), 0) + H_b(D(\mathbf{x}, \mathbf{x}_{ob}, \theta), \mathbf{x}_{ob}, 1) \quad (5.3)$$

$$H_b(p, q) = -q \cdot \log_2(p) - (1 - p) \cdot \log_2(1 - q) \quad (5.4)$$

Figure 5.4 shows some examples of generated UWA CIR samples during the training

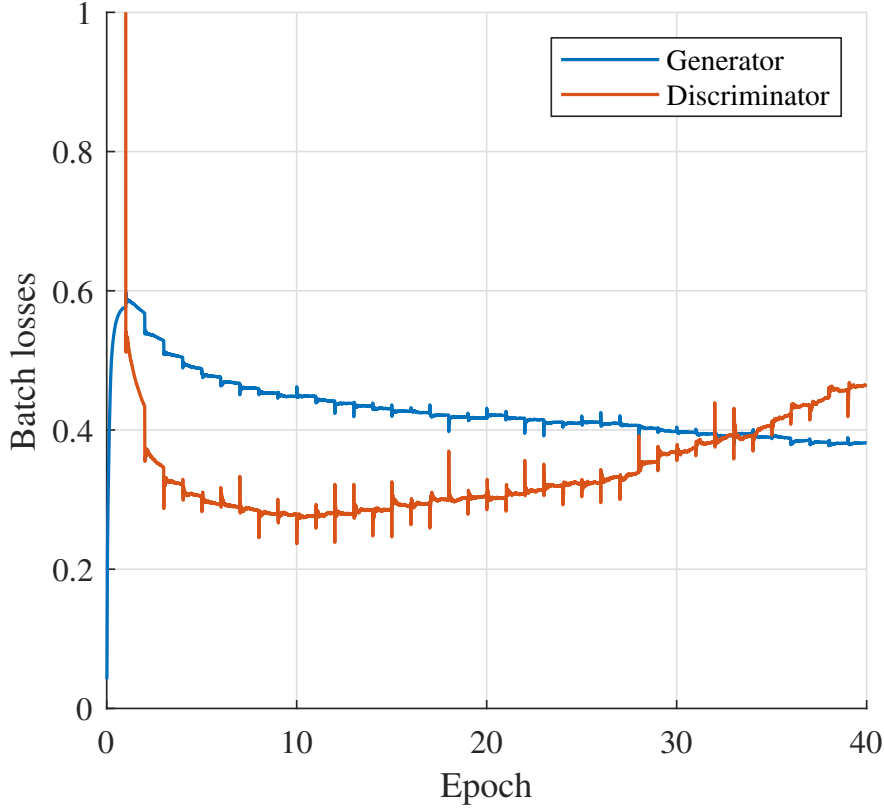


Figure 5.3: Batch losses during training

process. There are four different θ sequences are selected to demonstrate the generated CIR samples. The last θ vector of the sequence is printed on top of its corresponding CIR sample. The odd columns are the time domain amplitude of CIR samples, while the even columns are its corresponding frequency domain amplitude. The first row of Figure 5.4 are samples from the training data set. The second row is the corresponding CIR observations \mathbf{x}_{ob} in the training data set. The bottom three rows are three generated CIR samples with the same θ sequence and its corresponding CIR observations \mathbf{x}_{ob} . The generated samples show similarities to the training samples in both time and frequency domain amplitude plots. However, variations can also be

observed among the three generated samples, which indicates the prediction CGAN has the capabilities of avoiding the monotonousness of the stochastic replay of UWA CIR models.

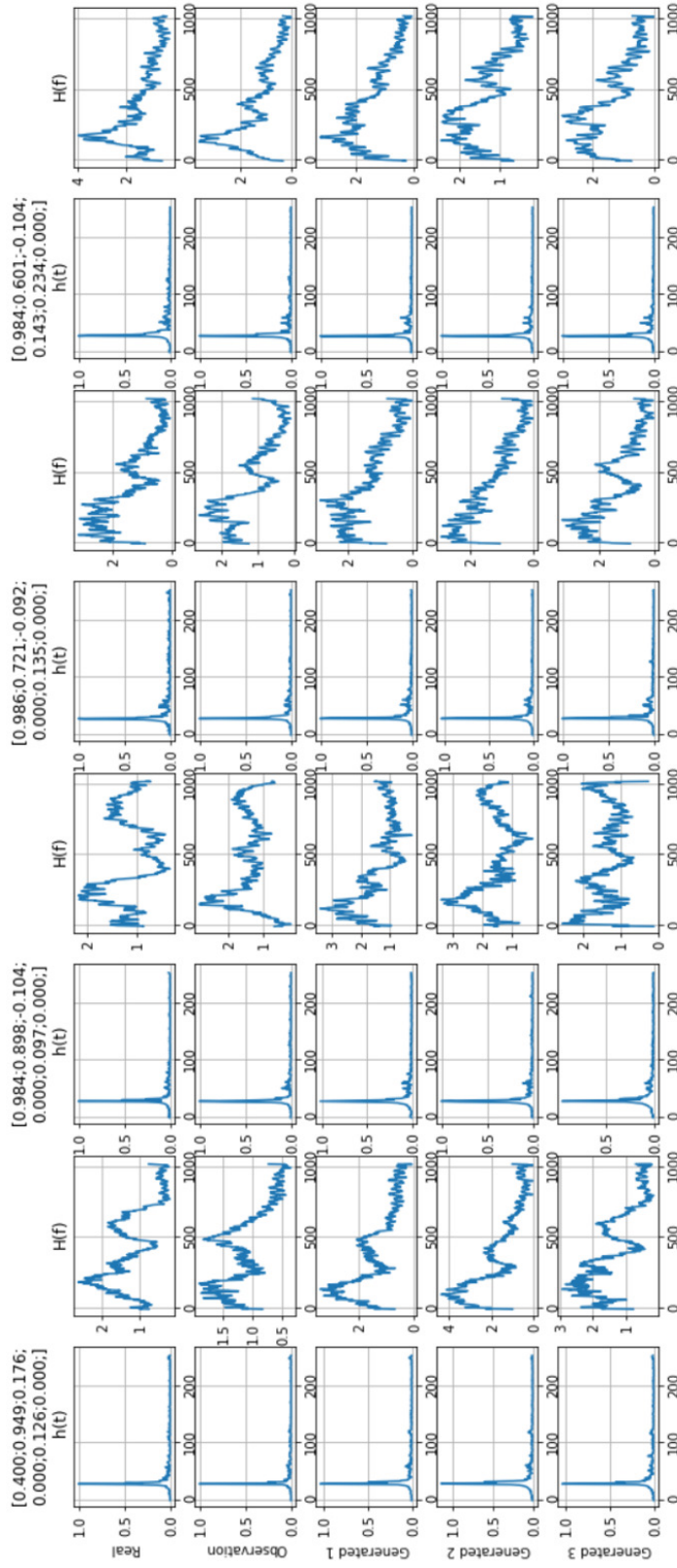


Figure 5.4: Generated samples during training

5.4 The prediction test results

The test data set consists of 161 time windows in three continuous time sections for the three cases discussed in Case Study 3.1 as shown in Figure 3.7. For the summer sunny days case, a series of 78 time windows for a continuous 24-hour period is selected as part of the test data set. There are also 36 time windows of a continuous 9-hour period for the summer cloudy case in the test data set, as well as 48 time windows of a continuous 12-hour period for the winter case.

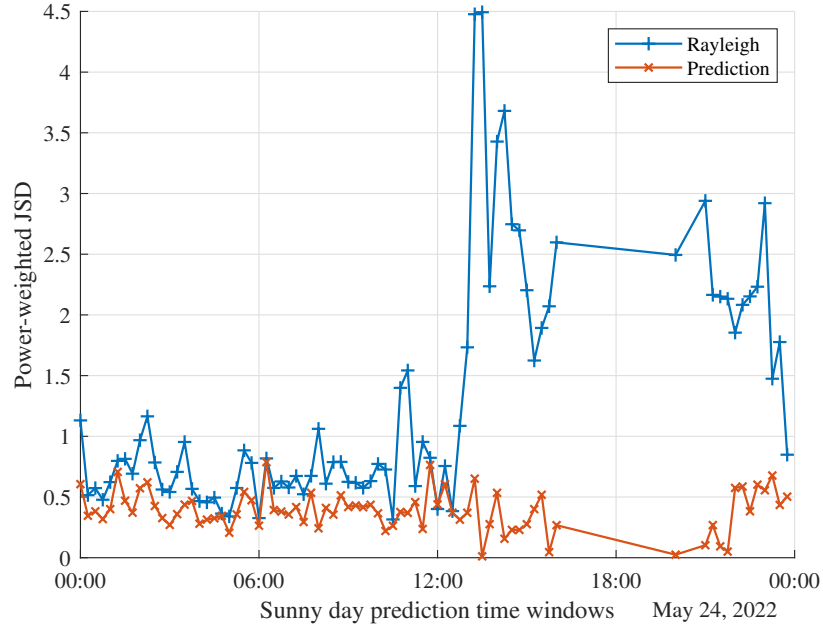


Figure 5.5: Power-weighted JSD of predictions in sunny day time windows

The θ sequence for the prediction test are generated in the same way as that of the training data set. However, the CIR observation \mathbf{x}_{ob} for all generated CIR samples

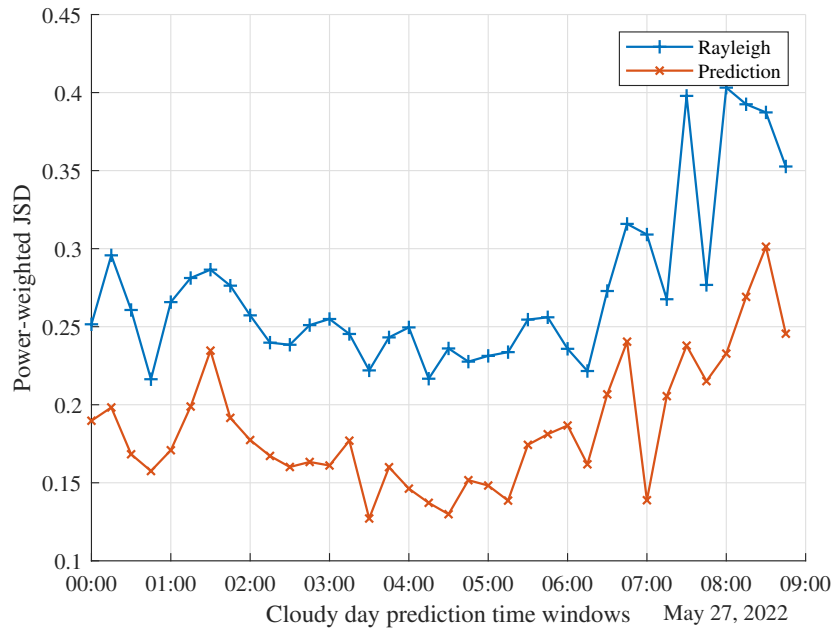


Figure 5.6: Power-weighted JSD of predictions in cloudy day time windows

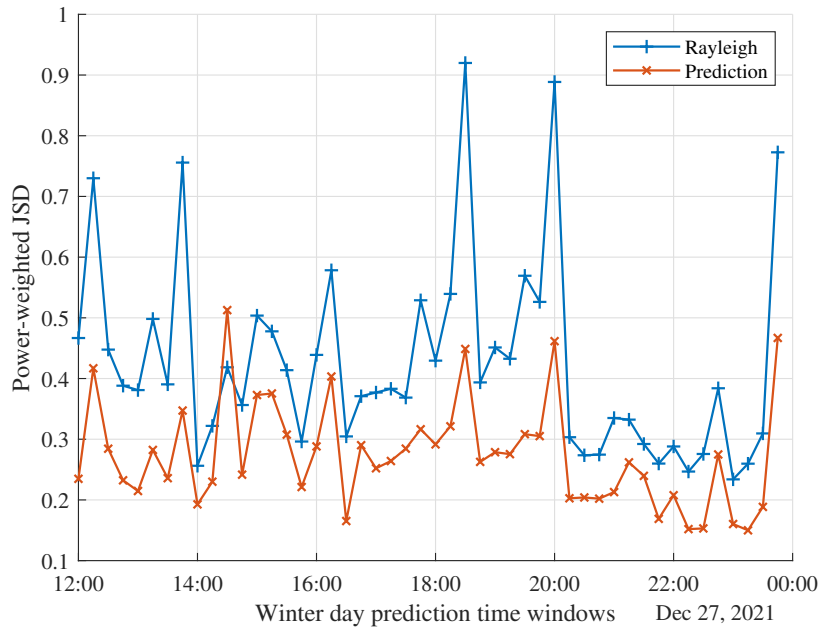


Figure 5.7: Power-weighted JSD of predictions in winter day time windows

within a time window is set as the first CIR sample of each test time window. The power-weighted JSDs of generated predictions for each test time window are compared with its Rayleigh fitting results in Figure 5.5 to 5.7. Especially for the summer sunny day case shown in Figure 5.5, the JSDs of Rayleigh fitting rapidly escalate after 12:00 due to the increasing water temperature variations at different depth, while the CGAN trained with other sunny day case data can still predict the CIR distributions with low JSDs that is similar to other time windows. The mean power-weighted JSDs of generated CIR distributions for different cases are shown in Table 5.3. The ResCGAN row refers to the generator with the residual network design as shown in the right figure of Figure 5.2, while the PredCGAN row refers to the pure MLP generator design as shown in the left figure of Figure 5.2. In Figure 5.8, the histograms of all JSDs in the 858 time windows are compared. Although the power-weighted JSDs of generated prediction results are not as small as the WCGAN cases, the proposed prediction CGAN also significantly outperforms the Rayleigh fitting results.

Table 5.3
Mean power-weighted JSDs of the predictions for different cases

Case Type	Training	Sunny	Cloudy	Winter	Mean
Rayleigh	0.4584	1.2767	0.2729	0.4259	0.5228
WCGAN	0.2636	0.3391	0.2036	0.2674	0.2679
ResCGAN	0.3160	0.5465	0.2298	0.2975	0.3322
PredCGAN	0.2780	0.3869	0.1848	0.2743	0.2835

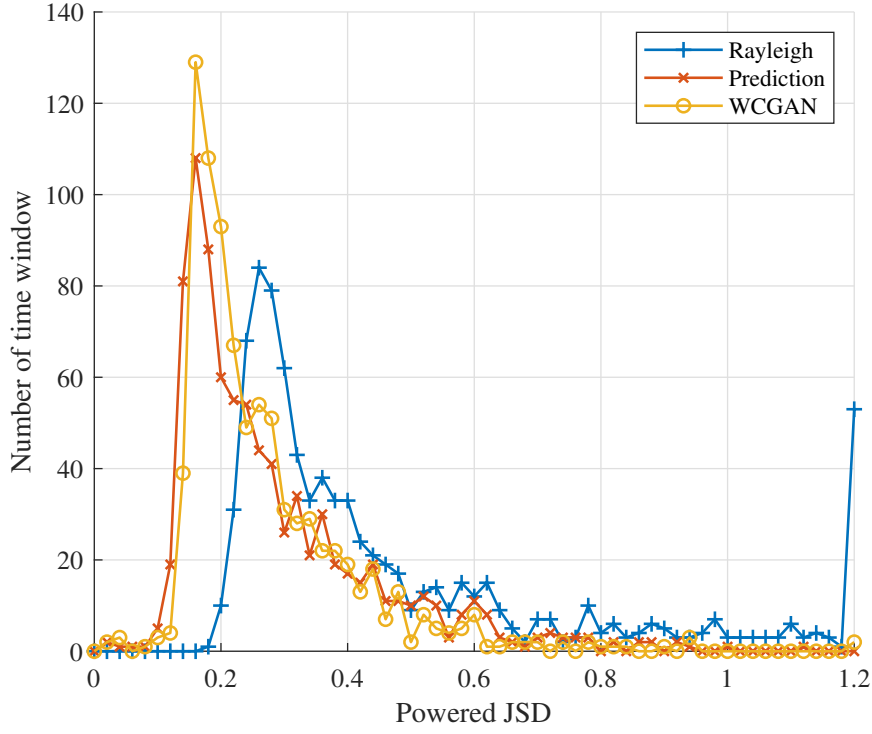


Figure 5.8: Histogram of power-weighted JSDs of the predictions, WCGAN generated, and fitted Rayleigh distribution

5.5 Summary of the prediction model

A CGAN model using a sequence of weather data and a recent CIR observation as the conditional inputs is proposed to perform the prediction of near-future UWA CIR distributions. The prediction results outperform the conventional stochastic distribution fitting method from the power-weighted JSD perspective.

Chapter 6

Conclusions and Future works

A low-cost field experiment system has been developed to conduct acoustic communication experiments and collect environmental data at a minute-level sampling rate. The proposed test-bed system can facilitate future field experiments to obtain more UWA data for deep learning research.

An ensemble of millions of OFDM waveform blocks has been collected with corresponding weather information in a series of field experiments. As discussed in the case studies, several observed phenomena show significant correlations between the UWA channel states and the environmental conditions. The obtained data set is a pioneer work for adapting deep learning models to solve UWA communication problems, and it can be proliferated with the help of the proposed test-bed system. The

minimum total amount and the minimum sampling rate of CIR samples for properly training a deep learning model can be explored and to modify the future field experiment designs.

A WCGAN model is proposed to learn the distribution of UWA CIR samples obtained in the field experiment. A power-weighted JSD measurement is proposed to evaluate the similarity of generated CIR distribution to the field experiment data distribution. The WCGAN outperforms conventional stochastic distribution fitting methods from the power-weighted JSD perspective.

The CIR distribution prediction for the cognitive UWA communication system is formulated as learning the CIR distribution conditioned on historical and future environmental data. A CGAN-based prediction model is proposed to generate CIR samples in a 15min near future based on a sequence of weather information and a recent CIR observation. The proposed CGAN prediction model performed better than classic stochastic distribution fitting methods on the test data set.

More advanced deep neural network architectures, such as the convolutional neural network, residual network, and attention mechanism, can be introduced to implement the WCGAN and the prediction models. Training techniques such as early stopping and learning rate decay can also be introduced to improve the performances of proposed deep learning models. The proposed generative models can be integrated with previous reinforcement learning models [77, 78] for adaptive UWA communications.

References

- [1] J. Mitola, *Cognitive radio*. PhD thesis, Institutionen för teleinformatik, 2000.
- [2] M. Stojanovic and J. Preisig, “Underwater acoustic communication channels: Propagation models and statistical characterization,” *IEEE communications magazine*, vol. 47, no. 1, pp. 84–89, 2009.
- [3] A. C. Singer, J. K. Nelson, and S. S. Kozat, “Signal processing for underwater acoustic communications,” *IEEE Communications Magazine*, vol. 47, no. 1, pp. 90–96, 2009.
- [4] A. Song, M. Stojanovic, and M. Chitre, “Editorial underwater acoustic communications: Where we stand and what is next?,” *IEEE Journal of Oceanic Engineering*, vol. 44, no. 1, pp. 1–6, 2019.
- [5] Z. Peng, S. Le, M. Zuba, H. Mo, H. Zhou, J.-H. Cui, S. Zhou, Z. Jiang, and J. A. Schindall, “Field test experience of an underwater wireless network in the atlantic ocean,” in *2013 MTS/IEEE OCEANS-Bergen*, pp. 1–10, IEEE, 2013.

- [6] I. F. Akyildiz, D. Pompili, and T. Melodia, “Challenges for efficient communication in underwater acoustic sensor networks,” *ACM Sigbed Review*, vol. 1, no. 2, pp. 3–8, 2004.
- [7] Z. Wang, S. Zhou, and Z. Wang, “Underwater distributed antenna systems: Design opportunities and challenges,” *IEEE Communications Magazine*, vol. 56, no. 10, pp. 178–185, 2018.
- [8] H. Song, S. Cho, T. Kang, W. Hodgkiss, and J. Preston, “Long-range acoustic communication in deep water using a towed array,” *The Journal of the Acoustical Society of America*, vol. 129, no. 3, pp. EL71–EL75, 2011.
- [9] L. Wei, Z. Wang, J. Liu, Z. Peng, and J.-H. Cui, “Power efficient deployment planning for wireless oceanographic systems,” *IEEE Systems Journal*, vol. 12, no. 1, pp. 516–526, 2016.
- [10] J. Younce, A. Singer, T. Riedl, B. Landry, A. Bean, and T. Arikan, “Experimental results with hf underwater acoustic modem for high bandwidth applications,” in *2015 49th Asilomar Conference on Signals, Systems and Computers*, pp. 248–252, IEEE, 2015.
- [11] Y. Luo, L. Pu, M. Zuba, Z. Peng, and J.-H. Cui, “Challenges and opportunities of underwater cognitive acoustic networks,” *IEEE Transactions on Emerging Topics in Computing*, vol. 2, no. 2, pp. 198–211, 2014.

- [12] W. Sun and Z. Wang, “Online modeling and prediction of the large-scale temporal variation in underwater acoustic communication channels,” *IEEE Access*, vol. 6, pp. 73984–74002, 2018.
- [13] T. C. Yang and S. H. Huang, “Building a database of ocean channel impulse responses for underwater acoustic communication performance evaluation: issues, requirements, methods and results,” in *Proceedings of the 11th ACM International Conference on Underwater Networks & Systems*, pp. 1–8, 2016.
- [14] J.-H. Cui, J. Kong, M. Gerla, and S. Zhou, “The challenges of building mobile underwater wireless networks for aquatic applications,” *Ieee Network*, vol. 20, no. 3, pp. 12–18, 2006.
- [15] I. Goodfellow, Y. Bengio, and A. Courville, *Deep learning*. MIT press, 2016.
- [16] S. Vagle, “Bubbles and acoustic communications experiment (space08): Acoustical and physical characteristics of diffuse bubble plumes,” tech. rep., INSTITUTE OF OCEAN SCIENCES SIDNEY (CANADA), 2008.
- [17] M. Taya, A. Tadayon, and M. Stojanovic, “Mobile acoustic communications: real data analysis of partial fft demodulation with coherent detection,” in *OCEANS 2018 MTS/IEEE Charleston*, pp. 1–7, IEEE, 2018.
- [18] P. A. van Walree, F.-X. Socheleau, R. Otnes, and T. Jensenrud, “The watermark benchmark for underwater acoustic modulation schemes,” *IEEE Journal of Oceanic Engineering*, vol. 42, no. 4, pp. 1007–1018, 2017.

- [19] C. Wang, Z. Wang, W. Sun, and D. R. Fuhrmann, “Reinforcement learning-based adaptive transmission in time-varying underwater acoustic channels,” *IEEE access*, vol. 6, pp. 2541–2558, 2017.
- [20] Q. Fu and A. Song, “Adaptive modulation for underwater acoustic communications based on reinforcement learning,” in *OCEANS 2018 MTS/IEEE Charleston*, pp. 1–8, IEEE, 2018.
- [21] J. Huang and R. Diamant, “Adaptive modulation for long-range underwater acoustic communication,” *IEEE Transactions on Wireless Communications*, vol. 19, no. 10, pp. 6844–6857, 2020.
- [22] C. Fan and Z. Wang, “Adaptive switching for multimodal underwater acoustic communications based on reinforcement learning,” in *The 15th International Conference on Underwater Networks & Systems*, pp. 1–2, 2021.
- [23] L. Wei, C. Fan, and Z. Wang, “An experimental study of underwater acoustic channel impulse response distributions in a river,” in *The 16th International Conference on Underwater Networks & Systems*, pp. 1–8, 2022.
- [24] H. Luo, K. Wu, R. Ruby, F. Hong, Z. Guo, and L. M. Ni, “Simulation and experimentation platforms for underwater acoustic sensor networks: Advancements and challenges,” *ACM Computing Surveys (CSUR)*, vol. 50, no. 2, pp. 1–44, 2017.
- [25] F. Campagnaro, R. Francescon, F. Guerra, F. Favaro, P. Casari, R. Diamant, and M. Zorzi, “The desert underwater framework v2: Improved capabilities and

- extension tools,” in *2016 IEEE Third Underwater Communications and Networking Conference (UComms)*, pp. 1–5, IEEE, 2016.
- [26] C. Petrioli, R. Petroccia, and D. Spaccini, “Sunset version 2.0: Enhanced framework for simulation, emulation and real-life testing of underwater wireless sensor networks,” in *Proceedings of the Eighth ACM International Conference on Underwater Networks and Systems*, pp. 1–8, 2013.
- [27] R. Martins, J. B. de Sousa, R. Caldas, C. Petrioli, and J. Potter, “Sunrise project: Porto university testbed,” in *2014 Underwater Communications and Networking (UComms)*, pp. 1–5, IEEE, 2014.
- [28] L. Wei, Z. Peng, H. Zhou, J.-H. Cui, S. Zhou, Z. Shi, and J. O’Donnell, “Long island sound testbed and experiments,” in *2013 OCEANS-San Diego*, pp. 1–6, IEEE, 2013.
- [29] L. M. Smith, J. A. Barth, D. S. Kelley, A. Plueddemann, I. Rodero, G. A. Ulses, M. F. Vardaro, and R. Weller, “The ocean observatories initiative,” *Oceanography*, vol. 31, no. 1, pp. 16–35, 2018.
- [30] S. N. Le, Z. Peng, J.-H. Cui, H. Zhou, and J. Liao, “Sealinx: A multi-instance protocol stack architecture for underwater networking,” in *Proceedings of the Eighth ACM International Conference on Underwater Networks and Systems*, p. 46, ACM, 2013.

- [31] B. Moridian, L. Wei, J. Hoffman, W. Sun, B. Page, M. Sietsem, Y. Zhang, Z. Wang, and N. Mahmoudian, “A low-cost mobile infrastructure for multi-auv networking,” in *2018 IEEE/OES Autonomous Underwater Vehicle Workshop (AUV)*, pp. 1–6, IEEE, 2018.
- [32] W. Sun, *Online Learning of the Spatial-Temporal Channel Variation in Underwater Acoustic Communication Networks*. PhD thesis, Michigan Technological University, 2019.
- [33] L. Wei, Y. Tang, Y. Cao, Z. Wang, and M. Gerla, “Exploring simulation of software-defined underwater wireless networks,” in *Proceedings of the international conference on underwater networks & systems*, pp. 1–5, 2017.
- [34] K. Kaur, J. Singh, and N. S. Ghumman, “Mininet as software defined networking testing platform,” in *International conference on communication, computing & systems (ICCCS)*, pp. 139–42, 2014.
- [35] T. R. Henderson, M. Lacage, G. F. Riley, C. Dowell, and J. Kopena, “Network simulations with the ns-3 simulator,” *SIGCOMM demonstration*, vol. 14, no. 14, p. 527, 2008.
- [36] N. McKeown, T. Anderson, H. Balakrishnan, G. Parulkar, L. Peterson, J. Rexford, S. Shenker, and J. Turner, “Openflow: enabling innovation in campus networks,” *ACM SIGCOMM computer communication review*, vol. 38, no. 2, pp. 69–74, 2008.

- [37] R. Fan, L. Wei, P. Du, C. Mc Goldrick, and M. Gerla, “A sdn-controlled underwater mac and routing testbed,” in *MILCOM 2016-2016 IEEE Military Communications Conference*, pp. 1071–1076, IEEE, 2016.
- [38] R. Fan, *Pushing the Limits of Wireless Sensor Networks-WSNs 20,000 Leagues Under the Sea*. University of California, Los Angeles, 2017.
- [39] S. Wang, Z. He, K. Niu, P. Chen, and Y. Rong, “New results on joint channel and impulsive noise estimation and tracking in underwater acoustic ofdm systems,” *IEEE Transactions on Wireless Communications*, vol. 19, no. 4, pp. 2601–2612, 2020.
- [40] G. Yang, Q. Guo, H. Ding, Q. Yan, and D. D. Huang, “Joint message-passing-based bidirectional channel estimation and equalization with superimposed training for underwater acoustic communications,” *IEEE Journal of Oceanic Engineering*, vol. 46, no. 4, pp. 1463–1476, 2021.
- [41] P. Qarabaqi and M. Stojanovic, “Statistical characterization and computationally efficient modeling of a class of underwater acoustic communication channels,” *IEEE Journal of Oceanic Engineering*, vol. 38, no. 4, pp. 701–717, 2013.
- [42] S. Zhou and Z. Wang, *OFDM for underwater acoustic communications*. John Wiley & Sons, 2014.
- [43] L. Wan, S. Tsai, and M. Almgren, “A fading-insensitive performance metric for a

- unified link quality model,” in *IEEE Wireless Communications and Networking Conference, 2006. WCNC 2006.*, vol. 4, pp. 2110–2114, IEEE, 2006.
- [44] Z. Wang, S. Zhou, G. B. Giannakis, C. R. Berger, and J. Huang, “Frequency-domain oversampling for zero-padded ofdm in underwater acoustic communications,” *IEEE Journal of Oceanic Engineering*, vol. 37, no. 1, pp. 14–24, 2011.
- [45] M. Menéndez, J. Pardo, L. Pardo, and M. Pardo, “The jensen-shannon divergence,” *Journal of the Franklin Institute*, vol. 334, no. 2, pp. 307–318, 1997.
- [46] T. Van Erven and P. Harremos, “Rényi divergence and kullback-leibler divergence,” *IEEE Transactions on Information Theory*, vol. 60, no. 7, pp. 3797–3820, 2014.
- [47] K. Yang, P. Xiao, R. Duan, and Y. Ma, “Bayesian inversion for geoacoustic parameters from ocean bottom reflection loss,” *Journal of Computational Acoustics*, vol. 25, no. 03, p. 1750019, 2017.
- [48] D. Foster, *Generative deep learning: Teaching machines to paint, write, compose, and play*. O’Reilly Media, 2019.
- [49] L. Wei and Z. Wang, “A variational auto-encoder model for underwater acoustic channels,” in *The 15th International Conference on Underwater Networks & Systems*, pp. 1–5, 2021.
- [50] P. C. Etter, *Underwater acoustic modeling and simulation*. CRC press, 2018.

- [51] R. Otnes, P. A. van Walree, and T. Jenserud, "Validation of replay-based underwater acoustic communication channel simulation," *IEEE Journal of Oceanic Engineering*, vol. 38, no. 4, pp. 689–700, 2013.
- [52] Z. Qin, H. Ye, G. Y. Li, and B.-H. F. Juang, "Deep learning in physical layer communications," *IEEE Wireless Communications*, vol. 26, no. 2, pp. 93–99, 2019.
- [53] H. Ye, L. Liang, and G. Y. Li, "Circular convolutional auto-encoder for channel coding," in *2019 IEEE 20th International Workshop on Signal Processing Advances in Wireless Communications (SPAWC)*, pp. 1–5, IEEE, 2019.
- [54] J. Guo, C.-K. Wen, S. Jin, and G. Y. Li, "Convolutional neural network-based multiple-rate compressive sensing for massive mimo csi feedback: Design, simulation, and analysis," *IEEE Transactions on Wireless Communications*, vol. 19, no. 4, pp. 2827–2840, 2020.
- [55] C.-K. Wen, W.-T. Shih, and S. Jin, "Deep learning for massive mimo csi feedback," *IEEE Wireless Communications Letters*, vol. 7, no. 5, pp. 748–751, 2018.
- [56] Z. Lu, J. Wang, and J. Song, "Multi-resolution csi feedback with deep learning in massive mimo system," in *ICC 2020-2020 IEEE International Conference on Communications (ICC)*, pp. 1–6, IEEE, 2020.

- [57] L. Liu, C. Oestges, J. Poutanen, K. Haneda, P. Vainikainen, F. Quitin, F. Tufveson, and P. De Doncker, “The cost 2100 mimo channel model,” *IEEE Wireless Communications*, vol. 19, no. 6, pp. 92–99, 2012.
- [58] T. J. OShea, T. Roy, and N. West, “Approximating the void: Learning stochastic channel models from observation with variational generative adversarial networks,” in *2019 International Conference on Computing, Networking and Communications (ICNC)*, pp. 681–686, IEEE, 2019.
- [59] M. Mirza and S. Osindero, “Conditional generative adversarial nets,” *arXiv preprint arXiv:1411.1784*, 2014.
- [60] M. Arjovsky, S. Chintala, and L. Bottou, “Wasserstein GAN,” *arXiv preprint arXiv:1701.07875*, 2017.
- [61] I. Gulrajani, F. Ahmed, M. Arjovsky, V. Dumoulin, and A. C. Courville, “Improved training of wasserstein gans,” *Advances in neural information processing systems*, vol. 30, 2017.
- [62] D. P. Kingma and J. Ba, “Adam: A method for stochastic optimization,” *arXiv preprint arXiv:1412.6980*, 2014.
- [63] W. Jiang and H. D. Schotten, “Neural network-based fading channel prediction: A comprehensive overview,” *IEEE Access*, vol. 7, pp. 118112–118124, 2019.

- [64] T. Wang, C.-K. Wen, S. Jin, and G. Y. Li, “Deep learning-based csi feedback approach for time-varying massive mimo channels,” *IEEE Wireless Communications Letters*, vol. 8, no. 2, pp. 416–419, 2018.
- [65] Y. Zhu, X. Dong, and T. Lu, “An adaptive and parameter-free recurrent neural structure for wireless channel prediction,” *IEEE Transactions on Communications*, vol. 67, no. 11, pp. 8086–8096, 2019.
- [66] C. Luo, J. Ji, Q. Wang, X. Chen, and P. Li, “Channel state information prediction for 5g wireless communications: A deep learning approach,” *IEEE Transactions on Network Science and Engineering*, vol. 7, no. 1, pp. 227–236, 2018.
- [67] D. Madhubabu and A. Thakre, “Long-short term memory based channel prediction for siso system,” in *2019 International Conference on Communication and Electronics Systems (ICCES)*, pp. 1–5, IEEE, 2019.
- [68] G. Liu, Y. Xu, Z. He, Y. Rao, J. Xia, and L. Fan, “Deep learning-based channel prediction for edge computing networks toward intelligent connected vehicles,” *IEEE Access*, vol. 7, pp. 114487–114495, 2019.
- [69] X. Li and H. Wu, “Spatio-temporal representation with deep neural recurrent network in mimo csi feedback,” *IEEE Wireless Communications Letters*, vol. 9, no. 5, pp. 653–657, 2020.

- [70] B. S. Shawel, D. H. Woldegebreal, and S. Pollin, “Convolutional lstm-based long-term spectrum prediction for dynamic spectrum access,” in *2019 27th European Signal Processing Conference (EUSIPCO)*, pp. 1–5, IEEE, 2019.
- [71] E. Brophy, Z. Wang, Q. She, and T. Ward, “Generative adversarial networks in time series: A survey and taxonomy,” *arXiv preprint arXiv:2107.11098*, 2021.
- [72] K. E. Smith and A. O. Smith, “Conditional gan for timeseries generation,” *arXiv preprint arXiv:2006.16477*, 2020.
- [73] Z. Li, C. Ma, X. Shi, D. Zhang, W. Li, and L. Wu, “Tsa-gan: A robust generative adversarial networks for time series augmentation,” in *2021 International Joint Conference on Neural Networks (IJCNN)*, pp. 1–8, IEEE, 2021.
- [74] G. Ramponi, P. Protopapas, M. Brambilla, and R. Janssen, “T-cgan: Conditional generative adversarial network for data augmentation in noisy time series with irregular sampling,” *arXiv preprint arXiv:1811.08295*, 2018.
- [75] C.-K. Lee, Y.-J. Cheon, and W.-Y. Hwang, “Studies on the gan-based anomaly detection methods for the time series data,” *IEEE Access*, vol. 9, pp. 73201–73215, 2021.
- [76] Z. Niu, K. Yu, and X. Wu, “Lstm-based vae-gan for time-series anomaly detection,” *Sensors*, vol. 20, no. 13, p. 3738, 2020.

- [77] C. Wang, L. Wei, Z. Wang, M. Song, and N. Mahmoudian, “Reinforcement learning-based multi-auv adaptive trajectory planning for under-ice field estimation,” *Sensors*, vol. 18, no. 11, p. 3859, 2018.
- [78] C. Wang, L. Wei, Z. Wang, M. Song, and N. Mahmoudian, “Reinforcement learning-based adaptive trajectory planning for auvs in under-ice environments,” in *OCEANS 2018 MTS/IEEE Charleston*, pp. 1–6, IEEE, 2018.
- [79] M. R. Khan, B. Das, and B. B. Pati, “Channel estimation strategies for underwater acoustic (uwa) communication: An overview,” *Journal of the Franklin Institute*, vol. 357, no. 11, pp. 7229–7265, 2020.
- [80] M. B. Porter, “The bellhop manual and users guide: Preliminary draft,” *Heat, Light, and Sound Research, Inc., La Jolla, CA, USA, Tech. Rep*, vol. 260, 2011.
- [81] G. Huang, Z. Liu, L. Van Der Maaten, and K. Q. Weinberger, “Densely connected convolutional networks,” in *Proceedings of the IEEE conference on computer vision and pattern recognition*, pp. 4700–4708, 2017.
- [82] D. P. Kingma and M. Welling, “Auto-encoding variational bayes,” *arXiv preprint arXiv:1312.6114*, 2013.
- [83] J. Tao, Y. R. Zheng, C. Xiao, and T. Yang, “Robust mimo underwater acoustic communications using turbo block decision-feedback equalization,” *IEEE Journal of Oceanic Engineering*, vol. 35, no. 4, pp. 948–960, 2010.

- [84] D. Li, D. Chen, J. Goh, and S.-k. Ng, “Anomaly detection with generative adversarial networks for multivariate time series,” *arXiv preprint arXiv:1809.04758*, 2018.
- [85] Y. Luo, X. Cai, Y. Zhang, J. Xu, *et al.*, “Multivariate time series imputation with generative adversarial networks,” *Advances in neural information processing systems*, vol. 31, 2018.
- [86] Z. Guo, Y. Wan, and H. Ye, “A data imputation method for multivariate time series based on generative adversarial network,” *Neurocomputing*, vol. 360, pp. 185–197, 2019.
- [87] Y. Luo, Y. Zhang, X. Cai, and X. Yuan, “E2gan: End-to-end generative adversarial network for multivariate time series imputation,” in *Proceedings of the 28th international joint conference on artificial intelligence*, pp. 3094–3100, AAAI Press, 2019.
- [88] Z. Niu, K. Yu, and X. Wu, “Lstm-based vae-gan for time-series anomaly detection,” *Sensors*, vol. 20, no. 13, p. 3738, 2020.